Oblique propagation of mountain waves to the upwind side of the Andes observed by GLORIA and ALIMA during the SouthTRAC campaign

Lukas Krasauskas[1], Bernd Kaifler[2], Sebastian Rhode[3], Jörn Ungermann[4], Wolfgang Woiwode[5], and Peter Preusse[6]

[1]Institute of Energy and Climate Research (IEK-7: Stratosphere), Forschungszentrum Jülich
[2]Institute of Atmospheric Physics, German Aerospace Center
[3]Forschungszentrum Jülich
[4]Institute of Energy and Climate Research - Stratosphere (IEK-7), Research Centre Jülich
[5]Karlsruhe Institute of Technology
[6]Juelich Research Center

November 22, 2022

Abstract

Gravity waves (GW) carry energy and momentum from troposphere to the middle atmosphere and have a strong influence on the circulation there. Global atmospheric models cannot fully resolve GWs, and therefore rely on highly simplified GW parametrizations that, among other limitations, account for vertical wave propagation only and neglect refraction. This is a major source of uncertainty in models, and leads to well-known problems, such as late break-up of polar vortex due to the "missing" GW drag around 60°S. To investigate these phenomena, GW observations over Southern Andes were performed during SouthTRAC aircraft campaign. This paper presents measurements from a SouthTRAC flight on 21˜September 2019, including 3-D tomographic temperature data of the infrared limb imager GLORIA (8-15 km altitude) and temperature profiles of the ALIMA lidar (20-80 km altitude). GLORIA observations revealed multiple overlapping waves of different wavelengths. 3-D wave vectors were determined from the GLORIA data and used to initialise a GW ray-tracer. The ray-traced GW parameters were compared with ALIMA observations, showing good agreement between the instruments and direct evidence of oblique (partly meridional) GW propagation. ALIMA data analysis confirmed that most waves at 25-40 km altitudes were indeed orographic GWs, including waves seemingly upstream of the Andes. We directly observed horizontal GW refraction, which has not been achieved before SouthTRAC. Refraction and oblique propagation caused significant meridional transport of horizontal momentum as well as horizontal momentum exchange between waves and the background flow all along the wave paths, not just in wave excitation and breaking regions.

Oblique propagation of mountain waves to the upwind side of the Andes observed by GLORIA and ALIMA during the SouthTRAC campaign

L. Krasauskas[1], B. Kaifler[2], S. Rhode[1], J. Ungermann[1,3], W. Woiwode[4], P. Preusse[1]

[1]Forschungszentrum Jülich, Institute of Energy- and Climate Research, Stratosphere (IEK-7), Jülich, Germany
[2]Deutsches Zentrum für Luft- und Raumfahrt, Institut für Physik der Atmosphäre, Oberpfaffenhofen, Germany
[3]JARA, Forschungszentrum Jülich GmbH, Jülich, Germany
[4]Karlsruhe Institute of Technology, Institute of Meteorology and Climate Research, Karlsruhe, Germany

Key Points:

- High-resolution multi-instrument measurements of orographic gravity waves over the Andes were carried out
- Oblique gravity wave propagation and strong horizontal refraction were observed and analysed using ray-tracing
- Significant redistribution of horizontal momentum due to horizontal refraction was observed all along the path of wave propagation

Corresponding author: Lukas Krasauskas, `l.krasauskas@fz-juelich.de`

Abstract

Gravity waves (GW) carry energy and momentum from troposphere to the middle atmosphere and have a strong influence on the circulation there. Global atmospheric models cannot fully resolve GWs, and therefore rely on highly simplified GW parametrizations that, among other limitations, account for vertical wave propagation only and neglect refraction. This is a major source of uncertainty in models, and leads to well-known problems, such as late break-up of polar vortex due to the ”missing” GW drag around 60°S. To investigate these phenomena, GW observations over Southern Andes were performed during SouthTRAC aircraft campaign. This paper presents measurements from a SouthTRAC flight on 21 September 2019, including 3-D tomographic temperature data of the infrared limb imager GLORIA (8-15 km altitude) and temperature profiles of the ALIMA lidar (20-80 km altitude). GLORIA observations revealed multiple overlapping waves of different wavelengths. 3-D wave vectors were determined from the GLORIA data and used to initialise a GW ray-tracer. The ray-traced GW parameters were compared with ALIMA observations, showing good agreement between the instruments and direct evidence of oblique (partly meridional) GW propagation. ALIMA data analysis confirmed that most waves at 25-40 km altitudes were indeed orographic GWs, including waves seemingly upstream of the Andes. We directly observed horizontal GW refraction, which has not been achieved before SouthTRAC. Refraction and oblique propagation caused significant meridional transport of horizontal momentum as well as horizontal momentum exchange between waves and the background flow all along the wave paths, not just in wave excitation and breaking regions.

Plain language summary

Gravity waves (GW) are temperature and wind disturbances in the atmosphere that carry energy and momentum from troposphere to the middle atmosphere and have a strong influence on the circulation there. Global atmospheric models currently cannot adequately represent GW propagation: the facts that GWs can change wave-front orientation (refraction) and travel horizontally (and not just vertically) are typically neglected. This leads to important known model inaccuracies, e.g. too low temperatures and too much ozone loss in southern polar regions. SouthTRAC aircraft measurement campaign observed GWs exited by wind flow over the Southern Andes in September-November 2019. Temperature measurements were conducted with the IR spectrometer GLORIA (provided 3-D data) and the ALIMA lidar instrument. GLORIA data revealed many overlapping waves of different wavelengths, their propagation further up was investigated using ray-tracing. Most waves seen by GLORIA were also observed by ALIMA as they propagated further up, instruments were in good agreement. We directly observed wave propagation in both vertical and horizontal directions and change in horizontal wave orientation (the latter was not seen before SouthTRAC campaign). Due to these phenomena, many GWs carried momentum that had different direction and was deposited in a different location than most models typically predict.

1 Introduction

Atmospheric gravity waves (GWs) are wind and air temperature perturbations for which gravity acts as the main restoring force (Fritts & Alexander, 2003). They are one of the main mechanisms of energy and momentum transport from the troposphere to the middle atmosphere and hence play a key role (Holton & Alexander, 2000; Fritts & Alexander, 2003) in middle atmosphere dynamics: GWs contribute to driving the Brewer-Dobson circulation (Alexander & Rosenlof, 2003) and the quasi-biennal oscillation (QBO) (Dunkerton, 1997; Ern et al., 2014), have an influence on the polar vortex (O’Sullivan & Dunkerton, 1995) and sudden stratospheric warmings (Ern et al., 2016; Thurairajah & Cullens, 2022) and can cause reversals of zonal mean jets in the mesosphere (Garcia & Solomon, 1985; McLandress, 1998). GW-induced drag also has an impact on the jet stream (Palmer et al., 1986; Ern et al., 2016), convection (Koch & Siedlarz, 1999; de la Torre et al., 2011; de Groot-Hedlin et al., 2017) and tropospheric weather systems (Kidston et al., 2015), and hence influence surface weather.

The most important GW sources include wind interaction with orography (e.g. Nastrom et al., 1987; Eckermann & Preusse, 1999), convection (e.g. Sato, 1993; Jiang et al., 2004), atmospheric fronts (Fovell et al., 1992; Ralph et al., 1999) and unstable jets (e.g. O'Sullivan & Dunkerton, 1995; Bühler, 1999; Plougonven & Zhang, 2014; Geldenhuys et al., 2021). Although conceptual models have been developed to understand and parametrize how these processes can emit GWs (e.g. Lott & Miller, 1997; Y. H. Kim et al., 2013; Charron & Manzini, 2002), there is still a large uncertainty in the amount of GWMF emitted and there are tuning parameters for emission efficiency and scales (e.g. Y.-J. Kim et al., 2003; Scinocca et al., 2008). Therefore one cannot deduce the relative strengths of various sources and their importance for the driving of the circulation in a straightforward way.

Gravity wave parametrizations are required because global circulation models (GCMs) and especially chemistry-climate models (CCMs) of the atmosphere cannot resolve significant parts of GW spectrum due to the prohibitive computational cost and rely on highly simplified parametrizations to account for GW activity. These parametrizations cannot accurately represent the spectrum, orientation or intermittency of the emitted GWs (e.g. McLandress, 1998; Alexander & Dunkerton, 1999; Scinocca & McFarlane, 2000; de la Camara et al., 2014), and typically assume purely vertical GW propagation, even though oblique GW propagation has been shown to occur by observations (Sato et al., 2003; Krisch et al., 2017), by statistical analysis of GW patterns (Jiang et al., 2004; Choi et al., 2009) and with modelling studies (Sato et al., 2009; Preusse et al., 2009; Kalisch et al., 2014). This can cause serious problems in the models. An example relevant to this study is the late break-up of the SH polar vortex ("cold-pole bias problem"; Butchart et al., 2011) present in most CCMs. It is widely believed to be caused by missing GW-induced drag around 60°S in GW parametrizations (e.g. McLandress et al., 2012), several different explanations involving orographic (e.g. Garcia et al., 2017) and non-orographic (e.g. Polichtchouk et al., 2018) sources were suggested and no consensus has been reached. More detailed, source-specific parametrizations have been proposed, but better observational data will be needed to constrain them (Plougonven et al., 2020).

Understanding the origins of observed GWs and attributing them to different sources and source locations is one way to better constrain GW modeling. However, this is still a difficult and rarely undertaken task (Wrasse et al., 2006; Hertzog et al., 2008; Pramitha et al., 2015; Geldenhuys et al., 2021), because it requires full characterisation of individual GWs, which cannot be accomplished by most observation techniques. Near-global coverage is provided by satellite instruments, but only nadir-viewing instruments are capable of delivering 3-D data products (AIRS; Hoffmann et al., 2016; Ern et al., 2017; Hindley et al., 2020). As they have poor vertical resolution they can detect only the long-wave part of the GW spectrum (larger than 15 km vertical wavelength for AIRS), which corresponds to very high intrinsic phase speed. Detectability of GWs hence depends largely on the background wind speeds. Despite such shortcomings, backward ray-tracing could be employed to infer orographic sources for GWs detected in the southern winter hemisphere (Perrett et al., 2021) and for mesoscale GWs emitted by the Hunga-Tonga eruption (Ern et al., 2022). Current limb-viewing satellites have excellent vertical resolution, but poor resolution along the line of sight (SABER: Russell III et al. (1999);HIRLDS: Gille et al. (2003)) and no across-track dimension. Therefore the propagation direction cannot be inferred and backward ray-tracing cannot be applied. Only forward modelling studies that make assumptions about source distributions and investigate propagation are possible (Ern et al., 2006; Preusse et al., 2009; Choi et al., 2009; Trinh et al., 2016). Full characterisation of the wave structure over a limited set of locations in the MLT region can be achieved using ground-based radar (MAARSY; Stober et al., 2013) or combinations of lidar and airglow measurements (e.g. Lu et al., 2015; Cao et al., 2016). A wave can also be fully characterised, if, for instance, the horizontal wave vector and the phase speed are known. This was used in the back-tracing studies of Wrasse et al. (2006) and Pramitha et al. (2015). Finally, the full 3-D wave vector can also be obtained using wind measurements from in situ instruments in radiosondes (e.g. Vincent & Alexander, 2000), superpressure balloons (Hertzog et al., 2008; Podglajen et al., 2016) and aircraft (e.g. Smith et al., 2016; Wagner et al., 2017), or from ground-based wind radar (PANSY; Minamihara et al., 2020). These wind measurements can be used to trace waves to their sources, but they have very limited spatial coverage. Generally, trajectory calculations are sensitive to small perturbations of the starting conditions. Their behaviour can be influenced by uncertainties of the atmospheric background conditions as well as the determination of the initial wave vector from the observations. In general, the GW source determination is most reliable at relatively low altitudes, e.g., in the lower stratosphere, and for waves that propagate steeply. More complex processes along the path of the ray, such as strongly oblique propagation and horizontal refraction (discussed in the following paragraph), enhance uncertainties. While successful back-tracing studies are reported, ray-traced waves were not previously observed at multiple locations along the ray path in order to validate the technique as such.

Horizontal refraction describes the change of the horizontal wave vector, which occurs as the wave propagates through horizontal wind gradients and is another often neglected aspect of wave propagation. This phenomenon can be predicted and quantified from the point of view of linear wave theory (Marks & Eckermann, 1995; Holton, 2004), previous studies focus on GW-permitting models (Chen et al., 2005; Hasha et al., 2008) or combine these models with ray-tracing (Strube et al., 2021). Due to the lack of observations that would allow to infer the wave propagation direction over various altitudes, no observational studies have been carried out before the SouthTRAC campaign (Geldenhuys et al., 2022, and this work). Despite this lack of observational evidence, substantial impact on the interaction of GWs with the background flow is expected: by changing the horizontal wave vector, horizontal refraction alters the amount and direction of the horizontal momentum carried by the wave and can hence result in significant redistribution of momentum along the path of wave propagation. This phenomenon is also mostly ignored in current GW parametrizations. Refraction also alters the overall direction of wave propagation and is therefore important for understanding oblique propagation in general. In order to validate these general theoretical concepts and motivate their application in global modelling approaches, we need an observational study, where all these aspects govern wave propagation and hence the distribution of the observed GW field.

In order to obtain observations of the same waves at various altitudes and to fully characterize the waves allowing ray-tracing, in the SouthTRAC (Southern Hemisphere Transport, Dynamics, and Chemistry) campaign two highly innovative instruments were deployed on the High Altitude LOng range (HALO) research aircraft of the German research community. The Gimballed Limb Observer for Radiance Imaging of the Atmosphere (GLORIA; Friedl-Vallon et al., 2014) is an airborne IR limb imager with the unique capability to provide high resolution 3-D temperature and trace gas data by observing an air mass from multiple directions and performing a 3-D tomographic retrieval, and is therefore ideally suited for in-depth analysis of GWs in the UTLS. GLORIA has been successfully used for GW (Krisch et al., 2017) and trace gas (Krasauskas et al., 2021) observations in the upper troposphere – lower stratosphere (UTLS) region. The second instrument is the Airborne LIdar for Middle Atmosphere research (ALIMA, see Section 2.2), which provides temperature data above the aircraft between the altitudes of 20 km and 80 km and thus shows how the waves observed by GLORIA propagate into the middle atmosphere. The SouthTRAC campaign was based in Rio Grande, Patagonia and several research flights were dedicated for the observation of oblique wave propagation and horizontal refraction.

In this paper, we present GW observations from a research flight over the Southern Andes, which was conducted on 20–21 September 2019 as part of the SouthTRAC measurement campaign (Rapp et al., 2020). On the day of the flight, SW wind over the Andes caused high amplitude orographic gravity wave activity, that was observed using GLORIA 3-D tomography and ALIMA data. Ray-tracing was used to link and compare the observations by the two instruments and to understand GW propagation and distribution in the region. We also compare our results to a simple mountain wave model (MWM), which was newly developed in Forschungszentrum Jülich.

Section 2 briefly describes the GLORIA and ALIMA instruments, their temperature retrieval techniques, our wave parameter fitting code, and the GROGRAT ray tracer that were used for data analysis, as well as ECMWF data used for model comparisons. The newly developed simple mountain wave model (MWM) is introduced at the end of the section. Section 3 presents the results and is subdivided as follows. Section 3.1 describes the meteorological conditions during observation. Section 3.2 presents GLORIA temperature data. Section 3.3 describes how wave parameters were obtained from GLORIA data and compared to ALIMA measurements. Gravity wave propagation over the Andes is then analysed in Section 3.4 using results from both instruments. Section 3.5 presents mountain wave model (MWM) results, as well as ECMWF, MWM and measurement data comparisons. Finally, conclusions are given in Section 4.

2 Methods and Data

2.1 The GLORIA Instrument and Retrievals

The Gimballed Limb Observer for Radiance Imaging of the Atmosphere (GLORIA) is an airborne IR limb imaging spectrometer. It records spectra in the 770 to 1400 cm^{-1} wave number range (Riese et al., 2005; Friedl-Vallon et al., 2014). In the applied configuration, GLORIA uses 128×48 effective pixels out of a 256×256 pixel detector array. GLORIA has a $1.5°$ field of view in the horizontal direction and $4°$ field of view in the vertical (typically $-3°$ to $1°$ elevation above the horizon). Infrared radiation along any line of sight comes mostly from the lowest point on the line of sight (called *tangent point*). Therefore, different line-of-sight elevations result in very different tangent point altitudes, allowing for very high vertical resolution of up to 200 m of the retrieved atmospheric quantities and a wide altitude range. The lower limit of observable altitude is around 5 km (due to clouds, aerosols, strong continuum emissions of water vapour below), and the upper limit is the flight altitude of the carrier aircraft (up to 15 km for the HALO aircraft used for this study).

GLORIA is a versatile instrument that can be used to observe air temperature and mixing ratios of multiple trace gases. In this paper, we will only consider 3-D tomographic temperature data used for studying GWs. For this type of measurement we use a short interferogram scan with a spectral sampling of 0.2 cm^{-1} and an acquisition time of $\approx$5 s. This is sufficiently fast for instrument panning, i.e. alternating the observation direction with respect to aircraft heading between 11 values in the $45°$ to $135°$ range. Panning allows to observe the same air mass from multiple directions, hence 3-D tomography is possible even using observations from a single straight flight leg, but such tomographic retrievals have lower resolution in the horizontal direction perpendicular to the flight track (Krisch et al., 2018, 2020). For best resolution in every direction, the aircraft needs to be flown around the observed air mass in a close-to-circular flight pattern with a diameter of around 200 km and also panning the instrument. Due to practical considerations, the actual tomography-optimised flight paths are typically hexagonal and around 400 km in diameter (Ungermann et al., 2010).

3-D retrievals are performed by means of inverse modelling, using the Jülich Rapid Spectral Simulation Code Version 2 (JURASSIC2). The radiative transfer model (Hoffmann et al., 2008) employed as the forward model uses the emissivity growth approximation method (Weinreb & Neuendorffer, 1973; Gordley & Russell, 1981) and the Curtis-Godson approximation (Curtis, 1952; Godson, 1953). A Newton-type trust region algorithm (Marquardt, 1963) and a conjugate gradients solver (Hestenes & Stiefel, 1952) are used for inverse modelling. Calculations were performed on an irregular grid with a Delaunay triangulation, using a Laplacian-based regularisation technique with physical parameters (Krasauskas et al., 2019). For more information about the 3-D tomography implementation refer to Ungermann et al. (2010, 2011); Krasauskas et al. (2019).

Table 1. Spectral windows for GLORIA 3-D temperature retrieval

#	Spectral range, cm^{-1}	#	Spectral range, cm^{-1}
1	791.0 - 793.0	6	980.0 - 984.2
2	863.0 - 866.0	7	992.6 - 997.4
3	892.6 - 896.2	8	1000.6 - 10006.2
4	900.0 - 903.0	9	1010.0 - 1014.2
5	956.8 - 962.4		

The temperature retrievals presented in this paper were performed using radiances from the spectral windows given in Table 1.

The retrieval also requires additional temperature and trace gas volume mixing ratio (VMR) data (called *a priori* data). It is needed to account for the IR radiation that various trace gases contribute to GLORIA observations and for retrieval regularisation (Krasauskas et al., 2019). GLORIA temperature data is not strongly affected by uncertainties in trace gas VMRs, as it relies heavily on IR emissions of CO_2, which is well-mixed in the atmosphere and has low uncertainties in its VMR. The a priori data for air temperature and pressure was taken from the European Centre for Medium-Range Weather Forecasts (ECMWF; Dee et al., 2011) operational analysis (T1279/L137 resolution). Whole Atmosphere Community Climate Model (WACCM; e.g. Garcia et al., 2007) data was chosen as a priori for O_3 and HNO_3. Since a priori data must be smooth (i.e. have no sharp transitions), reflect large-scale features of the relevant physical quantities and do not contain any perturbations due to GWs, a low-pass filter was applied to all a priori data sets. In particular, Savitzky-Golay filter (Savitzky & Golay, 1964) was used.

2.2 The ALIMA Instrument

The Airborne Lidar for Middle Atmosphere research (ALIMA) as flown during SouthTRAC is a compact upward pointing Rayleigh back-scatter lidar. It uses a frequency-doubled pulsed neodymium-doped yttrium aluminium garnet (Nd:YAG) laser with a mean optical output power of 12.5 W and 125 mJ pulse energy at 532 nm wavelength as light source. Back-scattered light is collected using a fibre-coupled 48 cm diameter Cassegrain telescope with a field of view of 330 µrad during lidar operation in darkness and 165 µrad in daylight. A set of three cascaded single-photon counting detectors covers the full dynamic range of the lidar return signal starting at about 5 km above the aircraft flight level to approximately 90 km altitude. In addition to reducing the telescope field of view, narrow-band optical filters (etalons) can be inserted in the receiver for enhanced rejection of the strong solar background when the lidar is operated in daylight.

Temperature profiles are retrieved by hydrostatic integration of the lidar back-scatter profiles in a similar way as for the ground-based CORAL instrument (Kaifler & Kaifler, 2021) at a cadence of one profile every two minutes, which corresponds to a horizontal resolution of 26 km assuming an aircraft speed of 220 m/s. The vertical resolution of the temperature profiles used in this study is 1500 m. For this 2 min × 1500 m resolution data set, typical uncertainties of the retrieved temperatures are 2.1 K within the altitude range of 30 km to 40 km and increase to 6.8 K in the 60 km to 70 km range.

2.3 S3D Wave Parameter Fitting Code

GW parameters (wave vector $\mathbf{k}$ and amplitudes) were determined from GLORIA 3-D temperature data using a small-volume few-wave decomposition method S3D (Lehmann et al., 2012), implemented as part of the JUWAVE gravity wave analysis software package developed in Forschungszentrum Jülich. The main idea of the method is to subdivide the measurement volume into smaller regions (rectangular boxes) and perform a least-squares fit in each of them, by minimizing

$$\chi^2 = \sum_i \left(T_i - \sum_j \left[A_j \sin\left(\mathbf{k}_j \cdot \mathbf{x}_i\right) + B_j \cos\left(\mathbf{k}_j \cdot \mathbf{x}_i\right) \right] \right), \tag{1}$$

where $\mathbf{x}_i$ and T_i are measurement data point positions and the respective residual temperature values at those points, $\mathbf{k}_j$ are the wave vectors, and A_j, B_j are wave amplitudes. The optimal $\mathbf{k}_j$ is found using variational methods, while A_j, B_j are determined analytically in every step of variation. In case the measurement data contains several different overlapping wave patterns, the fitting solution of the previous step is subtracted from the data and the fitting is repeated to obtain the parameters of the next wave pattern.

S3D was chosen for this work over the more common fast Fourier transform or wavelet methods, because it works well for small volumes of data and is not limited by a set of discrete frequencies. It has been shown (Lehmann et al., 2012; Preusse et al., 2012) to reliably determine wavelengths that range from one third to three times the size of the rectangular box in the corresponding dimension. Such capability is needed, since vertical wavelengths of many GWs discussed in this paper are actually larger than the usable vertical extent of GLORIA 3-D data, and the longest horizontal wavelengths span the whole 3-D tomography hexagon.

The horizontal gravity wave momentum flux (GWMF) for a monochromatic harmonic GW can be estimated from S3D results and some basic data about the state of the background atmosphere as follows (Ern et al., 2015):

$$(F_{px}, F_{py}) = \frac{\rho}{2} \left(\frac{g}{N} \right)^2 \frac{(k,l)}{m} \left(\frac{T_a}{T_0} \right)^2, \tag{2}$$

where ρ is air density, T_a is the temperature amplitude of the GW, T_0 is the mean temperature of the air mass the GW is propagating through, and wave vector is written as $\mathbf{k} = (k, l, m)$. If S3D data is used to initialise the GROGRAT ray tracer, GROGRAT provides GWMF data compatible with (2) along the ray path.

2.4 The GROGRAT Ray-Tracer

The Gravity wave Regional Or Global RAy Tracer (GROGRAT; Marks & Eckermann, 1995) was used for ray tracing the GWs observed by GLORIA and as part of the mountain wave model described in Sect. 2.5. The basics of GROGRAT operation can be described as follows. Let $\mathbf{x} = (x, y, z)$ and $\mathbf{k} = (k, l, m)$ be the position and wave vector of a GW packet, respectively. Then, denoting $\partial_\mathbf{a} \equiv (\partial/\partial a_x, \partial/\partial a_y, \partial/\partial a_z)$ for any vector $\mathbf{a} = (a_x, a_y, a_z)$, the ray tracing equations (Lighthill, 1978) can be written as

$$\frac{d\mathbf{x}}{dt} = \partial_\mathbf{k}\omega \qquad \frac{d\mathbf{k}}{dt} = -\partial_\mathbf{x}\omega, \tag{3}$$

where ω is the ground-based frequency, which GROGRAT determines from the GW dispersion relation

$$(\omega - Uk - Vl)^2 = \frac{N^2\left(k^2 + l^2\right) + f^2\left(m^2 + \alpha^2\right)}{k^2 + l^2 + m^2 + \alpha^2}. \tag{4}$$

Here $(U, V, 0)$ is the background wind, f – Coriolis parameter, N – Brunt-Väisälä frequency, and $\alpha \equiv 1/2H$, where H is the density scale height of the atmosphere. N and α are calculated from temperature background, which, along with the horizontal winds U, V, is obtained from smoothed-out ECMWF operational analysis data. The background data are processed in the same way as GLORIA a priori (see description in Section 2.1). Then, given the observed wave location $\mathbf{x}$ and wave vector $\mathbf{k}$, these quantities are calculated forwards and backwards in time. The evolution of GW amplitude along the ray path is obtained assuming conservation of wave action flux, dissipation by turbulent and radiative damping, and dissipation by saturation (for details, see Marks & Eckermann, 1995; Andrews et al., 1987). The ray tracing approximations remain valid as long as the Wentzel-Kramers-Brillouin approximation (WKB; Einaudi & Hines, 1970) holds. The latter condition ensures that relevant parameters of the background change sufficiently slowly in space and time. A violation of WKB would usually indicate a level where partial reflection occurs. Rays are terminated once the corresponding GWs reach a critical level, break down in amplitude or reach the altitude of 70 km.

2.5 Mountain Wave Model

The mountain wave model (MWM) estimates orography-induced GW activity based on the topography of the region being investigated. The model is inspired by the algorithm described by J. T. Bacmeister (1993); J. Bacmeister et al. (1994), but differs in the implementation of the ridge detection method. The calculation of GW distribution at a specific altitude in the atmosphere is implemented as follows. First, topography data is taken from the ETOPO1 1 arc-minute Global Relief Model (Amante & Eakins, 2009; Center, 2009), elevation is set to zero where data points are negative to approximate the sea surface. Then the MWM selects scales of interest by applying a Gaussian band pass filter to the topography. The filtered topography is further reduced to the arête lines by a gradient method, and straight ridge segments are identified from these by performing a probabilistic Hough transformation (e.g. Shapiro & Stockman, 2001). This provides a collection of lines with their respective positions, lengths and orientations, which is used for the positions of the mountain ridges. Idealised, Gaussian shaped ridges for these lines are fitted to the band pass filtered topography. In order to determine a GROGRAT ray launch distribution, the horizontal wavelength and displacement amplitude of GWs induced by flow over these idealised ridges are calculated as $\lambda_h = 4.9\sigma$ and $\zeta = h/2$ respectively, with σ being the width and h the height of the best fit Gaussian ridge (elevation $h \exp\left(-x^2/2\sigma^2\right)$, where x is the horizontal coordinate). The value of $\lambda_h/\sigma \approx 4.9$ has been estimated from fitting a Gaussian with width σ to a sine of corresponding wavelength λ_h. MWM implements flow blocking by reducing the effective height, and thus the displacement amplitude, of the mountain ridges to $\min(h, h_{\text{eff}})$, with $h_{\text{eff}} = U_{\text{perp}}/(NF_{\text{c}})$, where the tuning parameter $F_{\text{c}} = 4$ (e.g. Niekerk & Vosper, 2021). Time development of the mountain waves is predicted by passing the aforementioned GW parameters to the GROGRAT ray tracer and launching the rays hourly for the time period of interest.

The background fields used by the MWM for the ray tracing are ECMWF ERA5 hourly data (Hersbach et al., 2018; (C3S), 2017) with T639/L137 spatial resolution, interpolated to 130 equidistant height levels between 0 and 64.5 km with 0.3° horizontal sampling. A smooth large scale background was generated as described in Sect. 3.1.

3 Results and Analysis

3.1 Synoptic Situation and the Measurement Flight on 21 September

The region of Southern Andes is the strongest hotspot of stratospheric gravity wave activity on Earth (Hoffmann et al., 2016; Ern et al., 2018; Hindley et al., 2015). Typical conditions in this region during the austral spring include strong westerly winds from the Pacific interacting with the Andes and causing intense gravity wave excitation. Since the Southern Hemisphere polar vortex is usually more stable than the vortex in the Northern hemisphere, westerly winds typically prevail through most of the middle atmosphere, pro-

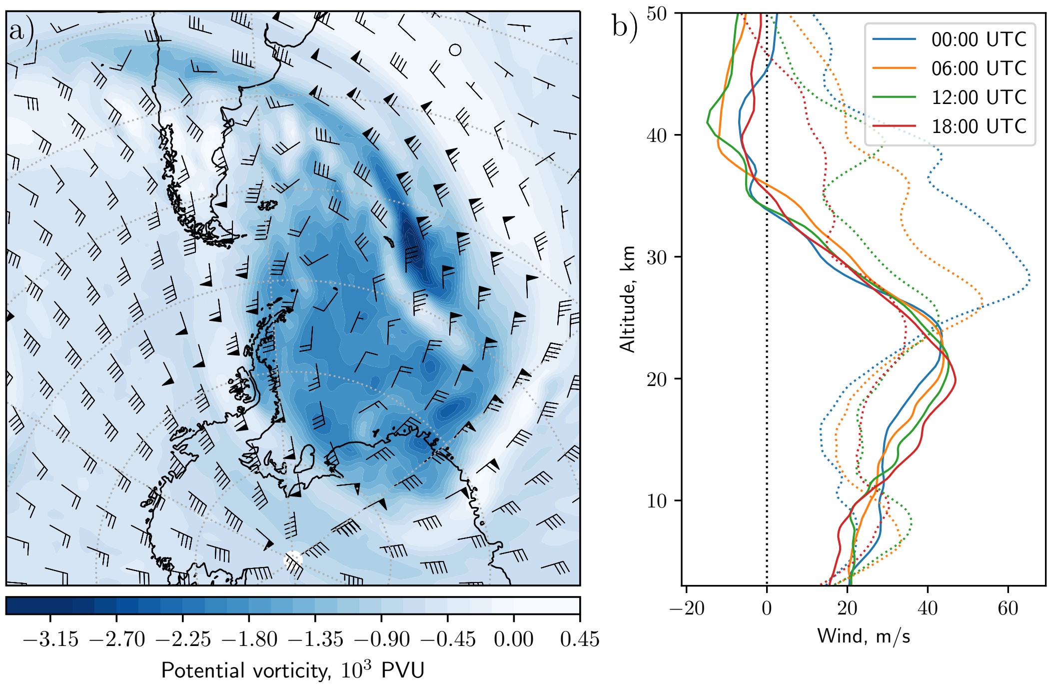

Figure 1. Both panels show ECMWF operational analysis data for 21 September. Panel a) – potential vorticity (PV) and winds for 35 km altitude at 06:00 UTC. Polar vortex can be identified with highly negative PV values. Wind velocity and direction is indicated by barbs (triangle represents 50 m/s , long barb 10 m/s, short barb 5 m/s). Panel b) – wind profiles over 50°S 73°W (center of the hexagonal flight pattern). Solid lines indicate zonal wind, dotted lines – meridional wind.

viding favourable conditions for the aforementioned gravity waves to propagate upwards all the way to the mesosphere. Studying these waves was one of the main goals of the SouthTRAC measurement campaign. The scientific flights of SouthTRAC dedicated to GWs were conducted 11th to 26th of September 2019 with the HALO aircraft operating from Rio Grande, Argentina. This coincided with a rare occurrence of a sudden stratospheric warming (SSW) in the Southern Hemisphere, that started in the end of August, with westerly wind velocities at 60°S, 10 hPa level reaching their minimum on 18 September (e.g. Rao et al., 2020), just three days before the measurement flight discussed in this paper. In the course of the SSW, the polar vortex was displaced from the pole and passing over the Andes at the time of measurement (Figure 1a). In the troposphere, south-westerly wind reached 30 m/s to 40 m/s and hence excited large-amplitude mountain waves (Figure 2a). However, the wind direction changed significantly with altitude in the stratosphere (Figure 1b), and waves encountered their critical levels at 35 km to 40 km altitude, where zonal wind changed direction. Orographic GWs cannot propagate above zero wind, either caused by a wind reversal or by winds becoming perpendicular to the wave vector.

While this synoptic situation did not allow for observation of GW propagation to the mesosphere with the ALIMA instrument, the complex wind pattern below the critical layer raised interesting questions. Before the measurement flight was executed, ECMWF forecasts showed GWs extending over the Pacific at the altitude of around 35 km, seemingly upwind of the Andes (Figure 2b, west of the coast around 47°S). This raised a question whether these were indeed orographic GWs, or whether they were excited by some other process. This will be further discussed in Sect. 3.4.

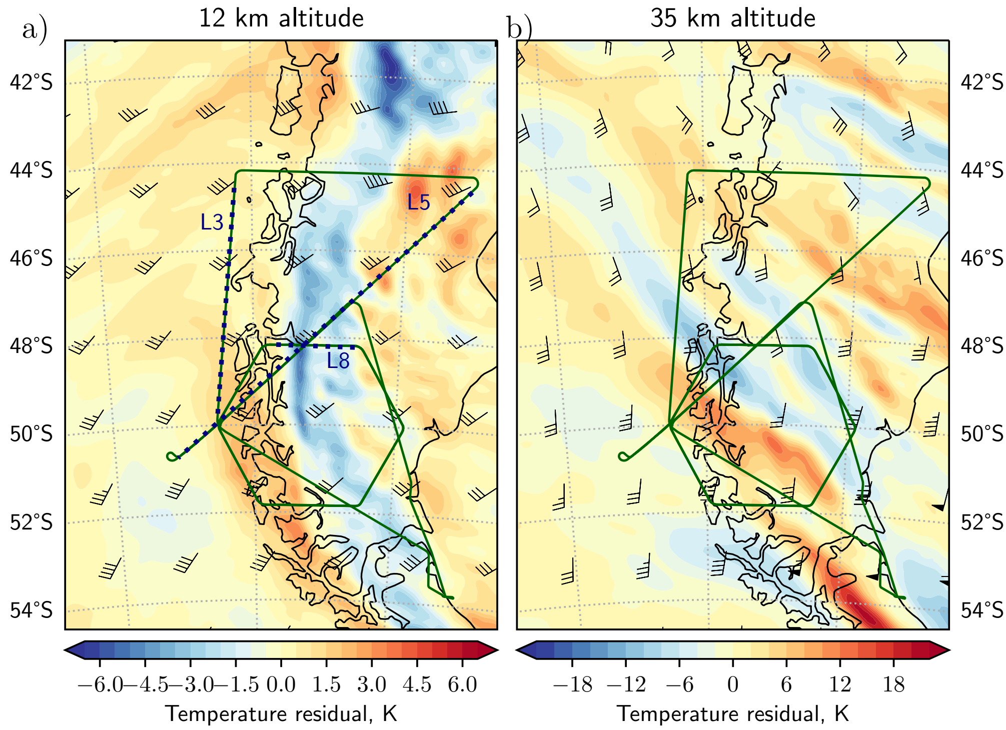

Figure 2. Both panels show ECMWF operational analysis detrended temperature (color scale) and wind (barbs) data over the Southern Andes for 21 September 2019, 06:00 UTC. The green line indicates the flight path of the HALO aircraft. Panel a) – horizontal cut at 12 km altitude; flight legs 3, 5 and 8 are highlighted by dark blue dots and labelled. Panel b) – horizontal cut at 35 km altitude. Wind barbs are defined as in Figure 1a.

The flight track of the measurement flight of 21 September is shown in Figure 2a. After take-off from Rio Grande, the HALO aircraft flew to the Pacific coast and observed air masses upwind of the Andes mountain range (flight segment labelled "L3" and marked by blue dots). The flight path then crossed the mountain range twice, the second crossing (segment "L5") being a long flight leg oriented against the wind at 25 km altitude and providing optimal conditions for ALIMA observations. The rest of the flight was used for encircling a 400 km stretch of the mountain range with a hexagonal flight pattern (Figure 2a, around 50°S 73°W) optimised for GLORIA 3-D tomographic retrieval, before heading back to the airport for landing. The hexagonal flight pattern was performed twice in order to capture temporal development as well. The first and second hexagon were flown at the (average) altitudes of 12.7 km and 13.4 km, respectively. A detailed study of time dependence of the temperature structures observed by GLORIA is outside the scope of the current paper and subject to further work. This paper focuses on understanding the general structure and propagation characteristics of the observed waves.

3.2 GLORIA 3-D Tomography

The large-scale structure of the GLORIA 3-D tomographic retrieval is presented in Figure 3, more detail can be seen in the 2-D cuts through the retrieval volume (Figure 4). Both figures show the GLORIA temperature data with a high-pass filter (Savitzky-Golay filter of order 3 with window width of 51 points (625 km), Savitzky and Golay (1964)) applied to isolate gravity waves. The region where the data is valid is roughly funnel-shaped and corresponds to the area covered by the limb sounding tangent points (see Section 2.1).

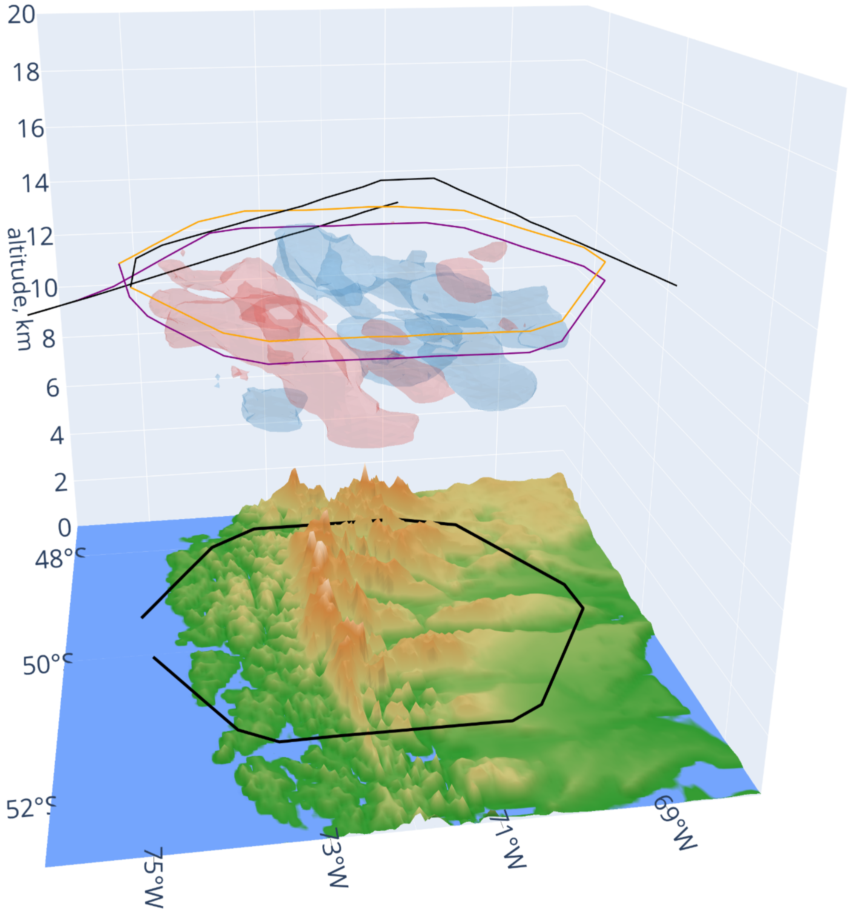

Figure 3. A 3-D visualisation of the large-scale temperature structure obtained from GLORIA tomographic retrieval. Blue and red isosurfaces show ±2 K residual temperature. The thick black line indicates the ground track of the hexagonal flight pattern. Flight tracks for the first and second hexagon are shown as orange and purple lines, respectively, the rest of the flight within the shown volume is represented by the thin black line.

Observations of the first hexagon (left-side panels of Figure 4) are valid at 03:42 UTC, those of the second hexagon (Figure 3 and right-side panels of Figure 4) are valid at 05:22 UTC (these are the time-wise midpoints of each hexagonal pattern, that took about 100 min each to execute). Our measurements reveal highly complex spatial temperature structure. We will identify the most important features and wave groups in the retrieved temperatures in this section, and continue with the more quantitative analysis based on least-squares fitting in Section 3.3.

The most prominent structure in the retrieved temperature is the large horizontal wavelength (about 350 km) gravity wave with phase fronts roughly parallel to the South American coastline. It manifests itself with high positive temperature residuals in the eastern side of the hexagon at 10 km altitude, negative temperature anomalies in the center (especially between 71.5°W and 73.5°W) and positive temperature residuals on the far eastern edge of the hexagon (the latter especially above 12 km altitude). This long wave accounts for most of the structure seen in Figure 3, and is in good agreement with ECMWF data (Figure 2), which shows a prominent warm-cold-warm feature of very similar length scale along the Andes. There is also a shorter wave (horizontal wavelength around 120 km) of similar orientation, highlighted with green dots in Figure 4c,d and clearly seen below 10.5 km altitude in Figure 4f. A slight change in the orientation of these waves with altitude is observed. Below about 11 km, phase fronts are aligned almost exactly in the North-South direction, while at higher altitudes a slight counterclockwise turn occurs (green dotted lines in Figure 4a-d). This will be discussed in terms of horizontal refraction in Section 3.4.

GLORIA data also reveals a group of waves with phase fronts oriented in approximately NW-SE direction, i.e. perpendicular to the wind. These waves have a lower amplitude, but can still be seen in Figure 4 (wave fronts marked with magenta dots in panels a-d, also seen in panels g,h).

Comparing data from the first and second hexagon (Figure 4, panels on the left and right, respectively) reveals some differences in wave front positions, wave amplitudes and the smallest scale waves, but no dramatic differences in temperature structure. This shows that the wave field did not undergo large changes over the period of flying both hexagons, and the instrument was indeed looking into similar structures from different directions during the course of flying each hexagon, i.e. the 3-D tomography concept is adequate. Detailed evaluation of the time evolution of the wave pattern is a subject of further work and is not considered here. GLORIA data along the flight path was also compared to in situ temperature measurements by the Basic HALO Measurement and Sensor System (BAHAMAS, Figure 5). The agreement between the two instruments is generally very good. Note that the horizontal resolution of GLORIA is about 20 km, and hence it cannot resolve temperature changes over time scales that are shorter than about 1.5 min (GLORIA horizontal resolution divided by flight speed) in Figure 5, which explains most of the differences. BAHAMAS data, however, suggests that there was significant short wave activity in the area that is inaccessible to GLORIA observations.

Finally, one must consider the effect of the tropopause on the GW structure in GLORIA data. The buoyancy frequency typically varies sharply with altitude close to the tropopause, and it follows from the dispersion relation (Eqn. 4) that this leads to rapid changes in the vertical wavelength, leading to a perturbed wave structure around the tropopause and potential partial reflection of GWs[1]. The tropopause height inside the hexagonal flight pattern was 8.5 km to 9 km, and one can indeed see the deformed wave fronts below 9 km in Figure 4f,h. The tropopause layer was therefore excluded from any wave fitting attempts, all the data about wave parameters was derived from altitudes above 9.25 km.

3.3 Ray Tracing and GLORIA-ALIMA Comparison

Our analysis of the GLORIA 3-D data from Section 3.2 identified GWs with a wide range of wavelengths. This is further supported by model and in situ data: Figure 2a shows a wave with horizontal wavelength of $\lambda_h \geq 500$ km being excited all along Southern Andes, while the periodic temperature disturbance detected at flight level by both GLORIA and BAHAMAS (Figure 5) suggests the presence of a GW with $\lambda_h \leq 65$ km. Recovering such a wide range of λ_h is challenging. Also, steep inclines of wave fronts in Figure 4 suggest large vertical wavelengths (λ_z), hence the full altitude range of GLORIA 3-D data from tropopause to flight altitude would be needed for the wave fitting. Therefore, for our main analysis, we chose to use data from the second hexagon (due to higher flight altitude) and chose the box size for the S3D wave parameter fitting algorithm to be 300 km × 300 km × 3.5 km, which will allow to reliably detect gravity waves with 100 km $< \lambda_h <$ 900 km, and 1.2 km $< \lambda_z <$ 10.5 km (see Section 2.3 for details on S3D). The waves with $\lambda_h <$ 100 km will be considered separately. Since the GLORIA 3-D retrieval grid has 12.5 km horizontal and 125 m vertical sampling, each S3D wave fitting box contains a subset of GLORIA grid of 25 × 25 × 29 grid points, a total of 18125 points. We used a total of 169 fitting boxes. The fitting boxes are centered at 11 km altitude, so that the box spans the altitudes from 9.25 km

[1] The GWs seen by GLORIA have intrinsic frequency too far from N to make total reflection relevant.

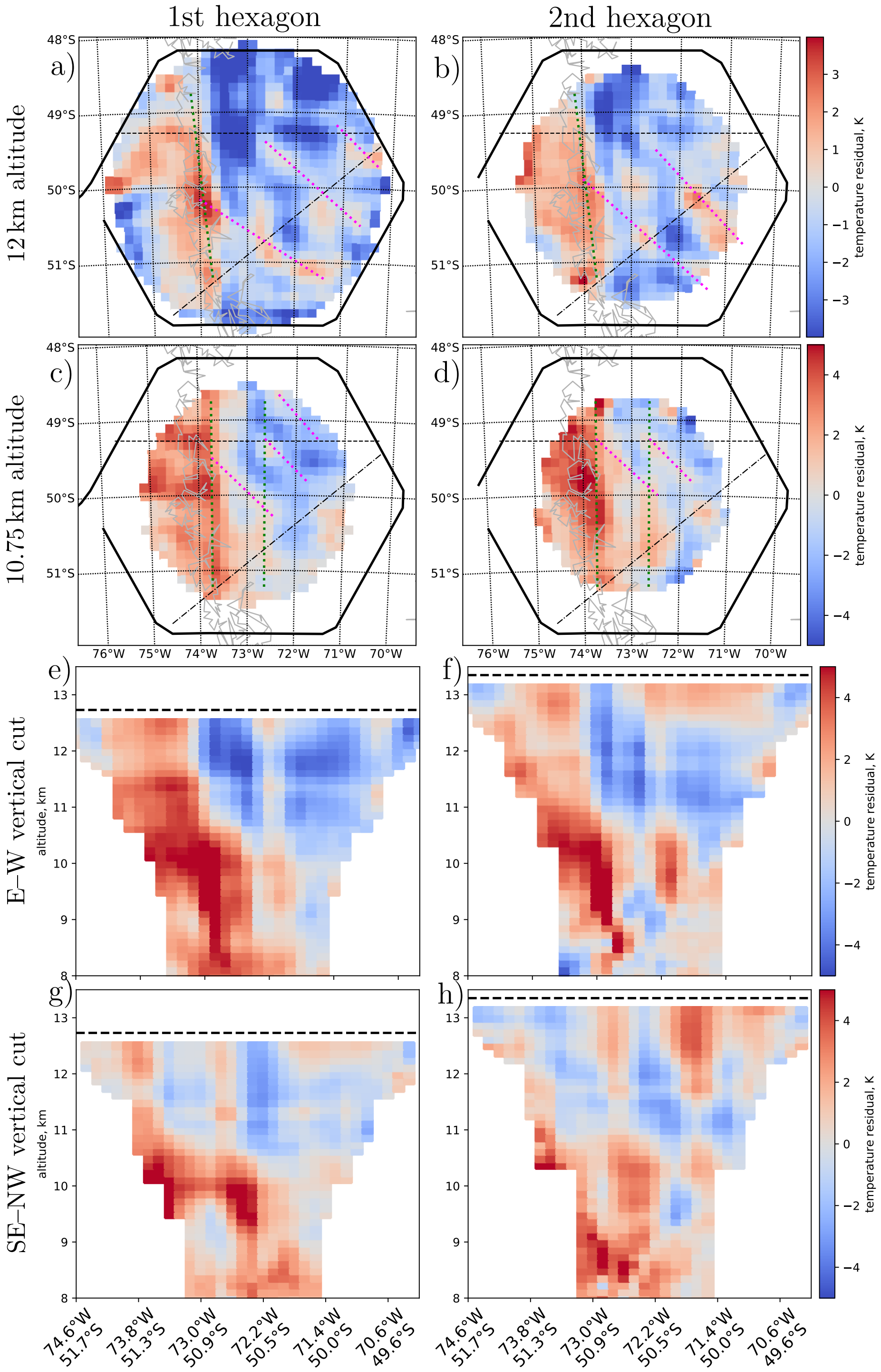

Figure 4. Temperature maps at 12 km altitude (panels a-b), maps at 10.75 km altitude (panels c-d) and vertical cuts (panels e-h) through GLORIA 3-D retrievals. Panels on the left and right present data acquired while flying the first and second hexagon, respectively. The thick solid black line shows the flight path, thick black dashes – flight altitude. Thin black dashes and dash-dots indicate the positions of vertical cuts shown in panels e-f, and the cuts shown in panels g-h, respectively. Colored lines mark various waves (see Section 3.2 of the main text).

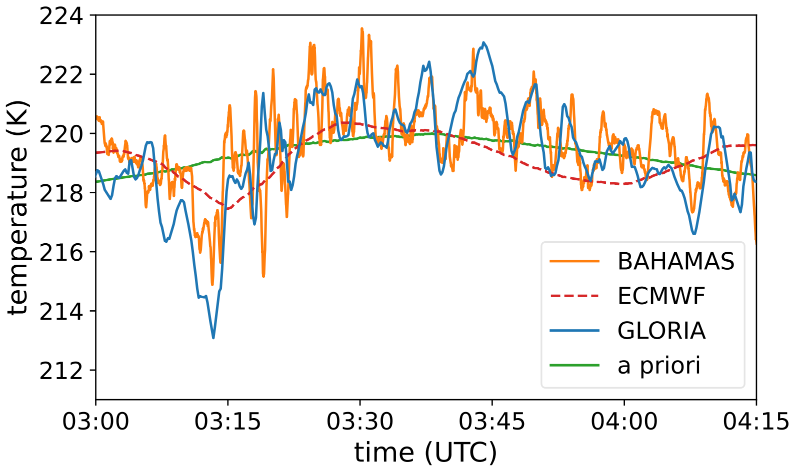

Figure 5. A comparison of GLORIA measurements along the flight track to in situ observations by BAHAMAS and ECMWF operational analysis. GLORIA retrieval a priori (cf. Sect. 2.1) is also shown.

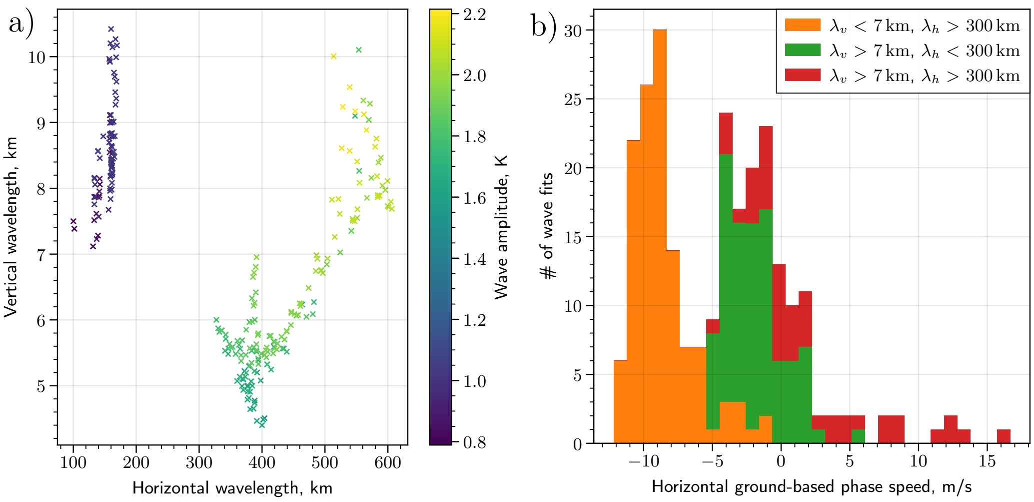

Figure 6. GW parameters determined by applying S3D to measurements from the second hexagon. Panel a) – horizontal and vertical wavelengths (λ_h, λ_z), as well as temperature amplitude (color coded) for each fit. Panel b) – distribution of fits with respect to ground-based horizontal phase speed. All valid fits fall into one of the three groups defined in the legend.

to 12.75 km. In the horizontal direction, cube centers form a 13 × 13 square grid, the center of this grid coincides with the center of hexagon. The spacing of this grid is 12.5 km, equal to the GLORIA data horizontal spacing. Therefore the boxes heavily overlap, and thus help to ensure that results are robust and not affected by possible localised GLORIA data artefacts or accidentally appearing periodic structures. Two waves were fitted for each cube.

S3D wave fitting results are presented in Figure 6. Out of the total 388 fits, there were 76 wave fits with $\lambda_z > 10.5$ km, these were excluded as unreliable (λ_z more than three times larger than the vertical fitting box dimension) and further 10 fits that were strong outliers in some other way (e.g. horizontal wave vector pointing in completely opposite direction to all other fits). All reliably-fitted GWs naturally fall into three groups based on horizontal and vertical wavelengths (see legend of Figure 6b).

The location of the hexagonal flight pattern (right over the mountain range and extending slightly into the leeward side) clearly suggests that the observed waves are of orographic origin. Further analysis is, however, needed to confirm this. Under constant winds, orographic waves should, in theory, be stationary waves, i.e. there should be no phase propagation with respect to the ground. In other words, the ground based phase speed $\mathbf{c}_p = \omega_{gb}\mathbf{k}_h/\|\mathbf{k}_h\|^2$ should be zero. In real life conditions, winds keep changing and GWs may also interact with cloud formation processes, resulting in non-zero $\mathbf{c}_p$ (Worthington, 1999). In spite of this, $c_p = \omega_{gb}/\|\mathbf{k}_h\|$ (i.e. projection of $\mathbf{c}_p$ in the direction of $\mathbf{k}_h$) is generally lower for orographic GWs compared to other source mechanisms and typically $|c_p| < 10\,\mathrm{m/s}$ (Strube et al., 2021). As seen in Figure 6b, the wave group with $\lambda_z > 7\,\mathrm{km}$, $\lambda_h < 300\,\mathrm{km}$ has c_p tightly distributed close to zero, and for the group with $\lambda_z < 7\,\mathrm{km}$, $\lambda_h > 300\,\mathrm{km}$ the distribution is similarly tight, but more offset towards the negative c_p values. These results indicate that both groups were mountain waves, but their phase lines were shifting at different rates due to wind change or interaction with clouds (GLORIA observed clouds within the hexagonal flight at the altitudes of up to 8 km). The wave group with $\lambda_z > 7\,\mathrm{km}$, $\lambda_h > 300\,\mathrm{km}$ is distributed over a wider range of c_p, but a large majority of the values are still compatible with an orographic source.

Another means of identifying GW sources from GW parameter fits is backward ray tracing from the observation location and verifying whether waves propagate from the direction of a mountain range. Backward ray tracing results are presented in Figure 7. It is clear that the waves with $\lambda_z > 7\,\mathrm{km}$ originate from the parts of the Andes mountain range directly below of the observation location and also mountains directly to the south of it. The backward trajectories of the waves with $\lambda_z < 7\,\mathrm{km}$, $\lambda_h > 300\,\mathrm{km}$ extend from the Pacific coast upstream of the Andes. It is important to note that the GROGRAT ray tracer determines only whether a GW can propagate at all and therefore the source may be located at any point along the backward trajectory, and not necessarily where it begins. In this case, there are no clear source regions, other than the Andes, to which waves with such low phase speeds at these altitudes could be attributed. Also, the waves in question are long enough to be resolved in ECMWF operational analysis data. S3D wave fitting was performed on ECMWF temperatures at multiple points over the Pacific along the backward trajectories shown here and no waves similar to the ones observed by GLORIA have been identified. All wave fits over the Pacific (west of 75°W) show $|c_p| > 20\,\mathrm{m/s}$ and a very different orientation of the horizontal wave number $\mathbf{k}_h$ compared to the group of GLORIA-observed waves considered here. This indicates that the waves observed by GLORIA with $\lambda_z < 7\,\mathrm{km}$, $\lambda_h > 300\,\mathrm{km}$ are excited over the Andes as well, but their properties are altered because of time-dependent phenomena (changing large-scale wind patterns), non-linear wave-wave interaction or cloud formation processes over the mountain chain.

The research flight considered in this work also provided the opportunity to follow one wave packet through a large range of altitudes and compare the GLORIA GW observations to those of the ALIMA lidar higher up. To that end, the GLORIA-data based S3D wave fits discussed above were used to initialise forward ray tracing with GROGRAT to investigate the propagation of the GLORIA-observed GWs after observation. Most of the resulting rays crossed the flight leg 5 (see Figure 2a for the location of leg 5 in the flight path) at the altitudes greater than 20 km, thus propagating through the atmospheric regions observed by ALIMA (Figure 8). This provided an opportunity to compare GLORIA and ALIMA measurements by direct comparison of GW wavelengths in ALIMA data and the wavelengths and directions of GLORIA-initialised GROGRAT rays where they intersect the ALIMA observations.

The ALIMA data from flight leg 5 were first detrended by computing the mean temperature profile (i.e. temperature as a function of altitude) for the whole flight leg, applying

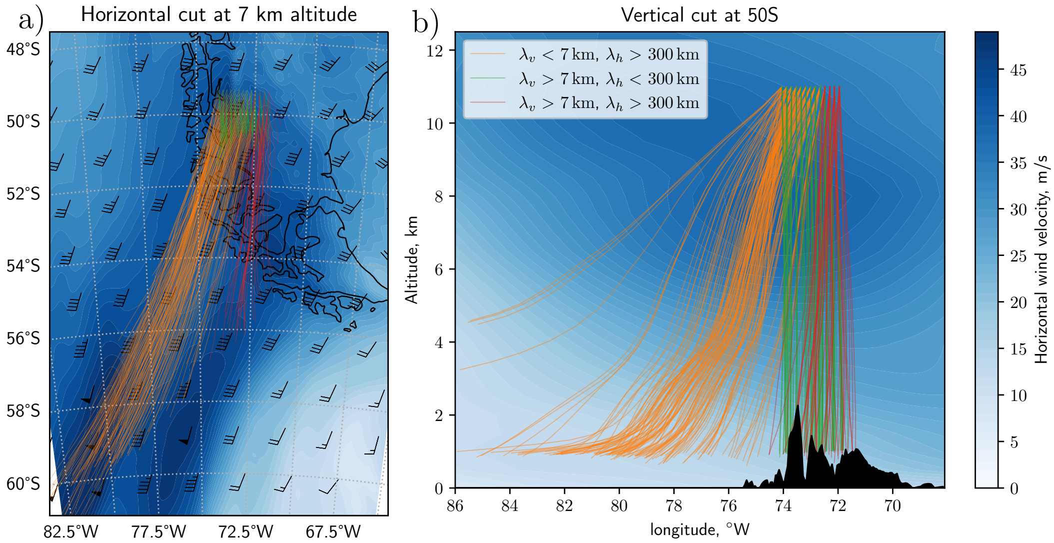

Figure 7. GROGRAT backward trajectories for the waves fitted to GLORIA 3-D data. Colored lines represent rays, color shading – horizontal wind velocity. Panel a) – horizontal map at 7 km altitude. Wind barbs as in Figure 1a. Refer to the legend and color bar of the panel b). Panel b) – ray projections onto a vertical cut through the atmosphere along 50°S parallel. Orography is shown in solid black.

a low-pass filter (Savitzky-Golay filter of order 3 with window width of 51 points (5 km), Savitzky and Golay (1964)) to the profile and subtracting the result from the temperature data. The resulting detrended temperature was used to compute the ALIMA GW spectrum[2] using 2-D continuous Morlet wavelet decomposition (Morlet et al., 1982; Torrence & Compo, 1998). Using this method one technically obtains a 2-D GW spectrum for each grid point on the ALIMA curtain[3]. The short-wavelength components of such a spectrum depend only on the temperature residuals close to that grid point, while the spectral components corresponding to longer waves are also influenced by temperature structures further away. In this paper, we will also discuss a GW spectrum in a certain region of ALIMA observations, which will be defined as the mean of the Morlet wavelet spectra for each point in the region. This way, a GW spectrum for wavelengths shorter than the region dimensions is defined almost entirely by the data within the region, while spectral components corresponding to longer wavelengths depend also on the data from region's surroundings.

The results of this comparison are presented in Figure 9. Figure 9a shows intersections of GW rays initialised from GLORIA data with the plane of ALIMA measurements from flight leg 5. The intersections are divided into four groups (c-f; marked in panel a) that are defined in terms of rectangular regions of the ALIMA curtain where the intersections take place. The corresponding spectra are then shown in panels c-f of Figure 9, respectively. The black points in the spectra indicate the wavelength values taken from the rays at the location of the intersection; the wavelength values are obtained by projecting the wave vector onto

[2] Strictly speaking, it is the spectrum of atmospheric GWs projected onto the vertical plane of ALIMA observations.

[3] Aspect ratio (i.e. ratio between horizontal and vertical spatial sampling for spectral analysis) was set to 40 to conform with the the mean of the typical ratios between horizontal and vertical GW wavelengths (e.g. Figure 6), 48 scales and 54 uniformly distributed wavelet orientations were used.

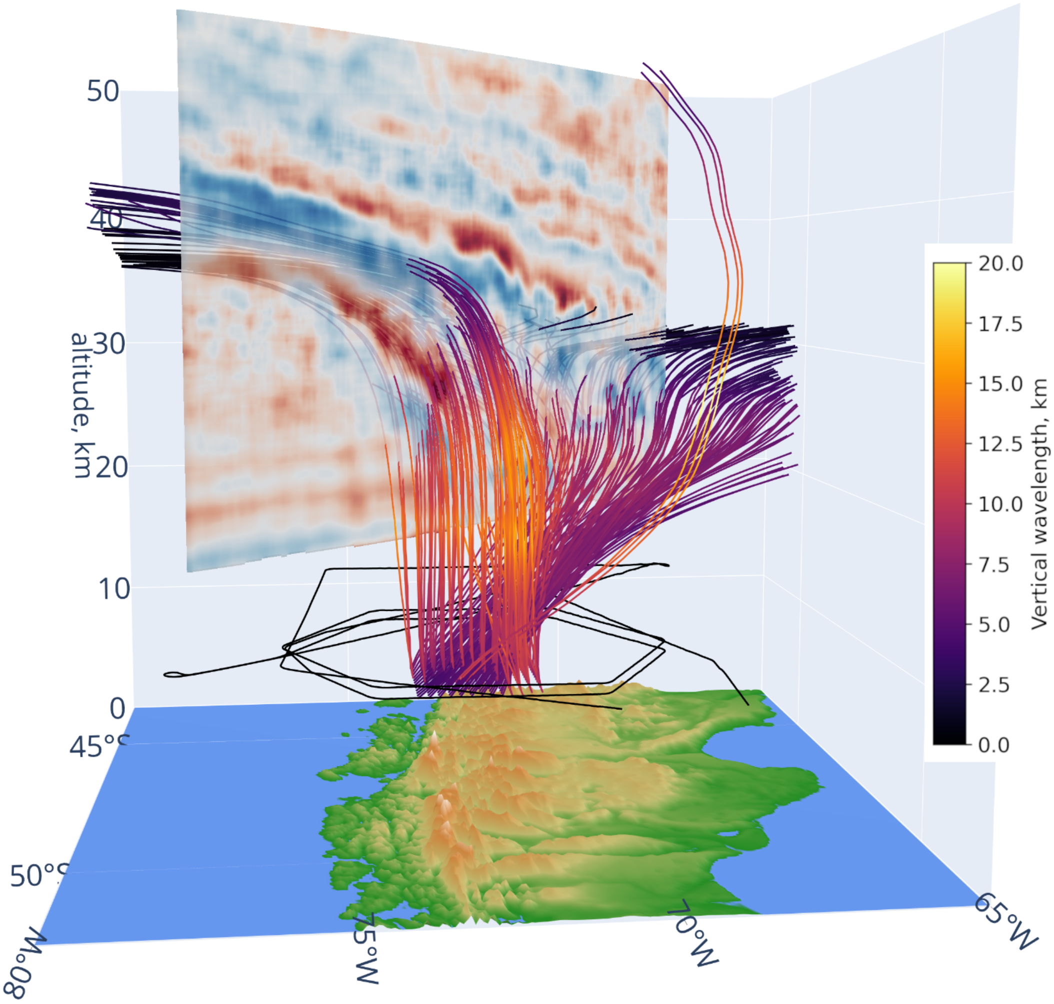

Figure 8. GROGRAT rays intersecting ALIMA measurement curtain over flight leg 5. Lines with color scale represent rays, black line – flight path.

the ALIMA curtain. All intersections, except for three outlying ones, fall into these four regions.

For the comparison it should be noted that flight leg 5 was flown just before the hexagonal flight pattern. In addition, the waves observed by GLORIA have a finite group velocity and thus took some time to reach the location of ALIMA observations. According to the ray-tracing data, the combination of both effects lead to a 5 h to 12 h time difference between the ALIMA observations and the most GLORIA-initialised rays reaching the same location (different rays intersect ALIMA observations at different altitudes, hence the wide time range).

Figure 9c shows the ALIMA GW spectrum from the rectangular region c depicted in Figure 9a, and the wavelengths of GLORIA rays crossing the ALIMA curtain in this area (horizontal wavelengths are projected to the plane of ALIMA observations). These rays represent GLORIA-observed waves of relatively long horizontal wavelengths (450 km to 600 km) and short vertical wavelengths (6 km to 7.5 km). This group demonstrates the most oblique propagation due to their relatively short vertical wavelength and wave front orientation: the wave vectors point west, i.e. around 45° from against-the-wind direction, resulting in relatively high ground-based horizontal group velocity and having long horizontal and short vertical wavelengths they have low vertical group velocity. Therefore, they cross the ALIMA curtain far inland and below 25 km altitude. There is a very good agreement between ALIMA data and wave parameters here, the rays clearly cluster at one of the two strongest ALIMA spectral peaks in the area.

Similarly, Figure 9d shows the ALIMA GW spectrum and ray crossings from rectangle d in Figure 9a. This group of rays starts with GLORIA-observed waves of long horizontal wavelengths same as the previous group, but propagates less obliquely and crosses the ALIMA measurement curtain higher, due to wave vectors oriented more opposite to the wind (deviation from wind direction down to 25°) and longer vertical wavelength (up to 8.8 km). The vertical wavelengths of these waves decrease as they approach 35 km altitude due to decreasing horizontal winds (Figure 9b, color scale shows winds at ALIMA measurement time, black contours – when GLORIA-initialized rays start crossing ALIMA curtain). This can be seen both on ALIMA data (the second spectral peak with vertical wavelengths around 5 km becomes prominent in this region) and ray crossings. Rays that cross the curtain below about 27 km altitude do so 8 h to 9 h after ALIMA measurement and have wavelengths in good agreement with the ALIMA spectrum. Rays that cross higher arrive up to 18 h after ALIMA measurement and, due to significant wind changes and a descending critical layer, have very short vertical wavelengths that do not agree with ALIMA which still measured at higher background wind conditions.

The short horizontal wavelength waves observed by GLORIA (seen as a clearly separate group in Figure 6a) cross the ALIMA curtain close to the Pacific coast, in regions e and f of Figure 9a. Due to their higher vertical wavelengths they propagate almost vertically before intersecting the ALIMA curtain and approaching the critical layer afterwards. Below 26 km altitude (Figure 9e) ALIMA data shows two partially overlapping spectral peaks around horizontal wavelengths of around 200 km and 120 km and data from GLORIA-initialised rays match excellently. Rays that intersect ALIMA curtain above 26 km (ray intersection region f) take up to 13 h to reach the curtain. Due to background wind changes as the waves propagate, GLORIA and ALIMA data do agree less well in Figure 9f.

Most significant spectral peaks in the ALIMA data are located in the white rectangles of Figure 9d (long horizontal wavelengths) and Figure 9e (short horizontal wavelengths). Therefore, one can use wavelet analysis to decompose the ALIMA data on flight leg 5 into two relatively coherent wave patterns (Figure 10) showing long and short waves. Both patterns show clear evidence of vertical refraction due to vertical gradients in wind velocities and sharp decreases in wave amplitude around their critical layers. Maximal amplitudes of short waves roughly coincide with the areas where the GLORIA rays of corresponding characteristics propagate, which suggests that most of the shorter waves seen in this ALIMA curtain originate from the stretch of the Andes inside the GLORIA hexagon or close to it. However, the long wave pattern observed by ALIMA (Figure 10a) is probably excited by the whole mountain range.

In comparing GLORIA and ALIMA observations, one must remember that GLORIA only observed waves over a small portion of the Andes mountain range, and these waves propagated in various directions. Similarly, any given region of ALIMA observations can contain waves excited at different points along the mountain range, some of them previously observed by GLORIA, some not. Therefore, we formulate two conditions for GLORIA and ALIMA observations to be consistent with one another. Firstly, GLORIA-initialised ray parameters should correspond to some peak in ALIMA spectrum at the location where they cross the region of ALIMA observations. This condition alone would already show good agreement. However, on top of it, we can formulate an additional condition that makes our claims stronger. Namely, all major peaks appearing in the ALIMA spectrum as a whole should have corresponding GLORIA-initialised rays somewhere on the ALIMA

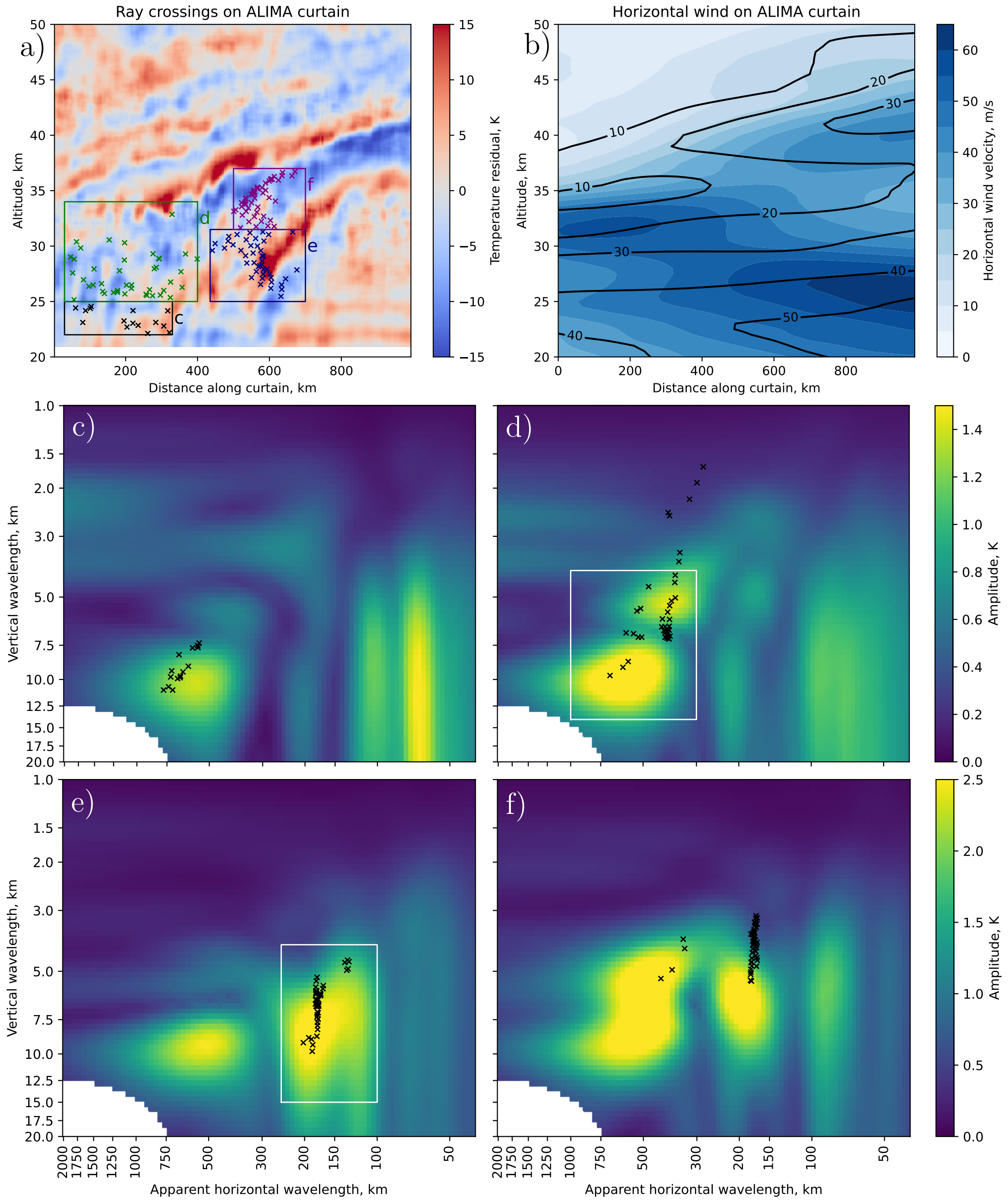

Figure 9. Comparison of ALIMA data and GW parameters obtained from GLORIA data-initialised ray tracing. Panel a) – ALIMA air temperature residuals from flight leg 5. Distance along the curtain is measured from the starting point (north-western end) of the flight leg, hence the direction of increasing distance is NE to SW. Crosses indicate locations where rays cross the curtain. All intersections (except for three) were located in the rectangles labelled c-f. Panel b) – horizontal wind velocity along the ALIMA curtain. Color scale and black contours show winds from 03:00 UTC and 12:00 UTC, 21 September, respectively. Panels c-f show ALIMA GW spectra for the rectangles in panel a labelled with corresponding letters. Black crosses indicate the wave parameters of the intersecting rays (horizontal wavelengths projected to ALIMA curtain). White rectangles in panels d and e depict spectral regions reconstructed in Figure 10 a and b, respectively.

curtain [4]. Based on Figure 9 and the corresponding discussion above, the first condition is met, and we believe that the second is met as well, because the most prominent structures in ALIMA spectrum are the two double peaks marked by white rectangles in the figure (which correspond to slightly different wavelengths depending on location on ALIMA curtain), and each of them have matching GLORIA-initialised rays (one peak at regions c and d, the other in the region e). We hence claim that the two instruments are in very good agreement.

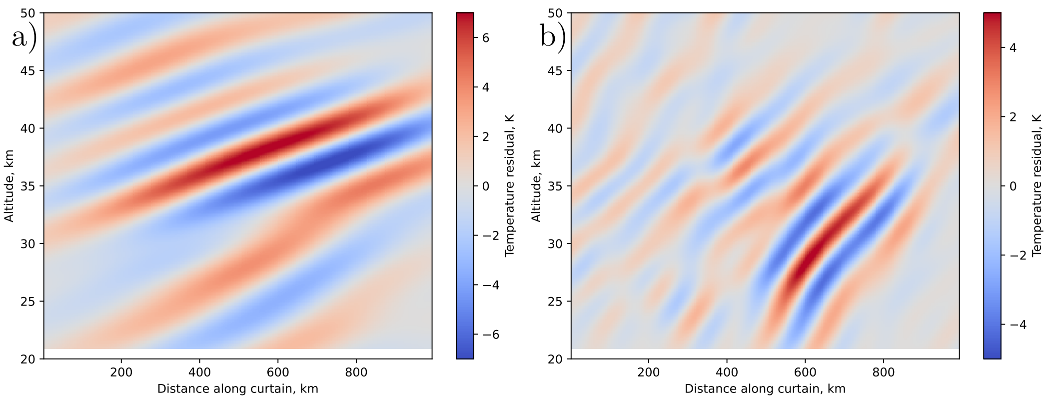

Figure 10. Panels a and b show temperature residuals for the flight leg 5, reconstructed from spectral regions depicted by white rectangles in Figure 9d and e, respectively.

The S3D wave fitting run used to initialise all the ray tracing introduced up to this point used fitting boxes measuring 300 km × 300 km × 3.5 km. Therefore, this run is not well suited for detecting wave packets with a horizontal extent below about 200 km and waves with $\lambda_h < 100$ km. However, such waves are seen in GLORIA temperature data in Figure 4. Also, almost all the S3D fits had wave vectors pointing in the direction between W and WSW (not shown), while GLORIA temperature structures indicate GWs with wave vectors pointing to the SW (cf. dotted magenta lines in Figure 4a,b). Therefore, a separate S3D run for fitting short waves was performed. In order to remove also the longer scale GWs before applying S3D, a 2D Fast Fourier Transform (FFT) high-pass filter was applied to GLORIA data to remove all waves with $\lambda_h > 150$ km. The resulting temperature residuals were used for an S3D fitting box measuring 100 km × 100 km × 3.5 km, which allows to detect waves with 33 km $< \lambda_h <$ 300 km, and 1.2 km $< \lambda_z <$ 10.5 km (see Section 2.3 for details on S3D). Due to the limits of GLORIA's horizontal resolution and the high-pass filter described above, we actually expect to see waves with 50 km $< \lambda_h <$ 150 km.

The parameters of the fitted waves are presented in Figure 11a. A dominating horizontal wavelength of ≈80km is found, which is in good agreement with previous findings from (Alexander & Barnet, 2007). The wave parameters were used to initialise the GROGRAT ray tracer and perform a comparison with ALIMA data, same as for the long-wavelength S3D fit. For comparison, ALIMA data from flight leg 8 (shown on a map in Figure 2a) was used this time, as a large number of rays cross the ALIMA curtain acquired why flying this leg (Figure 11b). Also, being part of the hexagonal flight pattern, leg 8 allows to minimize the time interval between ALIMA measurements and the time when GLORIA-initialised rays reach ALIMA curtain. Finally, Figure 12 compares GLORIA and ALIMA results in the same way as it was done in Figure 9.

[4] But at any given small region of ALIMA observations there might be some spectral peaks without matching GLORIA observations, in case ALIMA sees some waves excited at the Andes outside the GLORIA hexagon, and the waves from the hexagon with similar parameters simply crossed ALIMA curtain elsewhere.

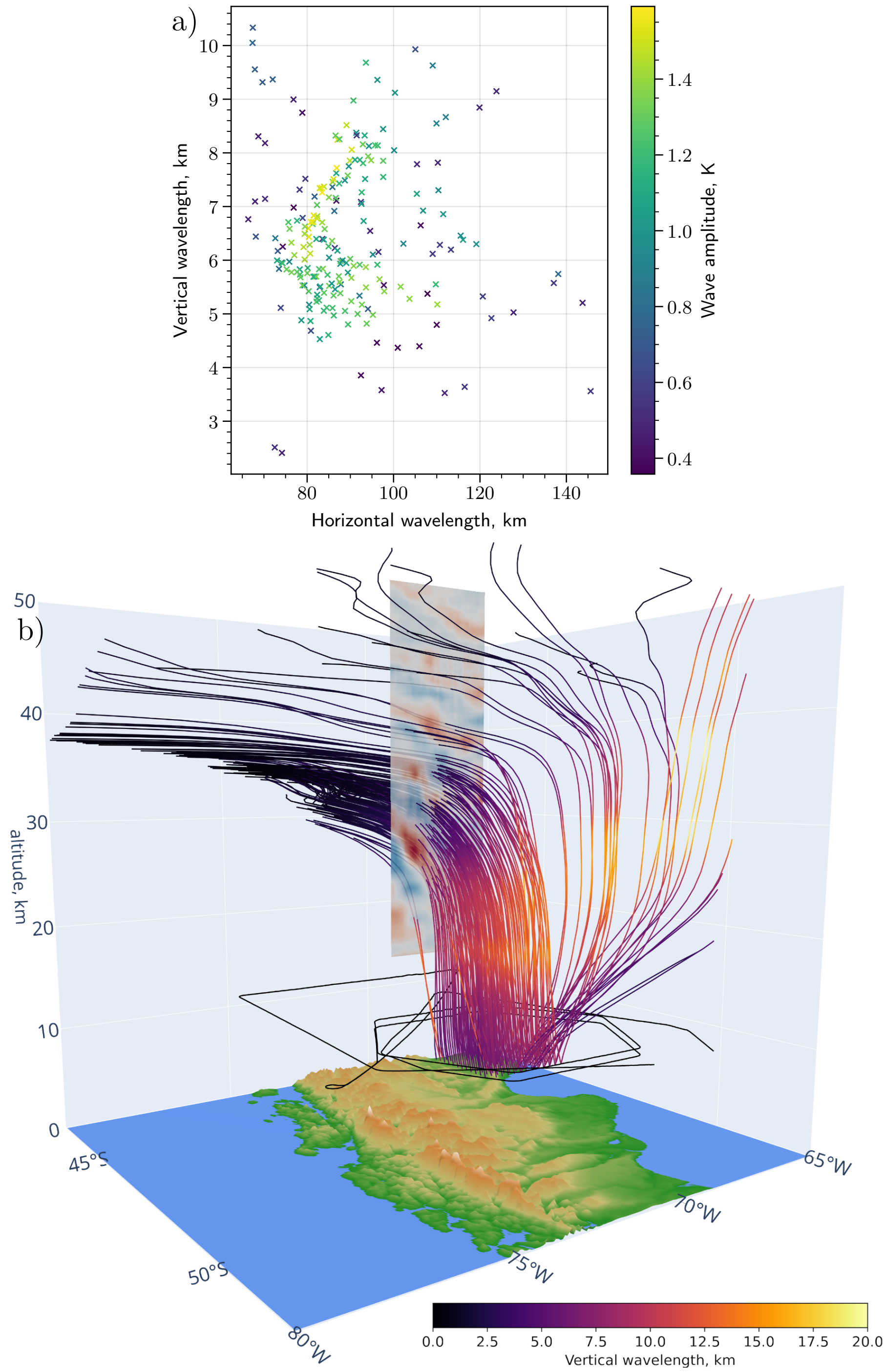

Figure 11. Panel a) – GW parameters determined using S3D short-wave fit from measurements of the second hexagon. Color scale shows wave amplitudes. Panel b) – GROGRAT rays initialised from short-wave S3D fit intersecting ALIMA measurement curtain over flight leg 8 (hexagon flight leg). Lines with color scale represent rays, black line – flight path.

As one can see in Figure 11a, the high-amplitude wave fits cluster in the spectral region with 70 km $< \lambda_h <$ 100 km, and 5 km $< \lambda_z <$ 8 km. These waves follow similar trajectories to the shorter waves of the previous fit (group c in Figure 9a, and Figure 9c), initially propagating almost vertically, and then, when approaching the critical level, turning northwards or towards NW. The ALIMA spectrum below 30 km altitude (group b in Figure 12a, and Figure 12b) is dominated by short waves with the same wavelengths as GLORIA-initialized rays, demonstrating an very good match between the two instruments[5]. Above 30 km altitude, the ALIMA spectrum is dominated by waves with larger λ_h (Figure 12c), but there are still some lower amplitude disturbances that match GLORIA data. Finally, there is a group of rays initialized from wave fits with initial wave vectors pointing in directions between WSW and SW (all the other fits have wave pointing between W and WSW). These waves cross the ALIMA curtain above 35 km altitude (group d in Figure 12a, and Figure 12d) having followed more complicated trajectories (Figure 11b). They match a minor peak in the ALIMA spectrum.

In summary, we have validated GLORIA and ALIMA data against each other and found that all wavelengths from GROGRAT ray-paths matched a major spectral peak in the ALIMA spectra, thus showing excellent agreement except where the background winds did change significantly in the time period between ALIMA measurements and the moment when the waves observed by GLORIA arrived at the same location. Also, every major peak in the ALIMA spectrum correspond to some GLORIA-initialised rays. As GLORIA temperature structures were shown to consist of mountain waves, also the major part of the wave pattern observed by ALIMA hence can be explained by mountain wave activity.

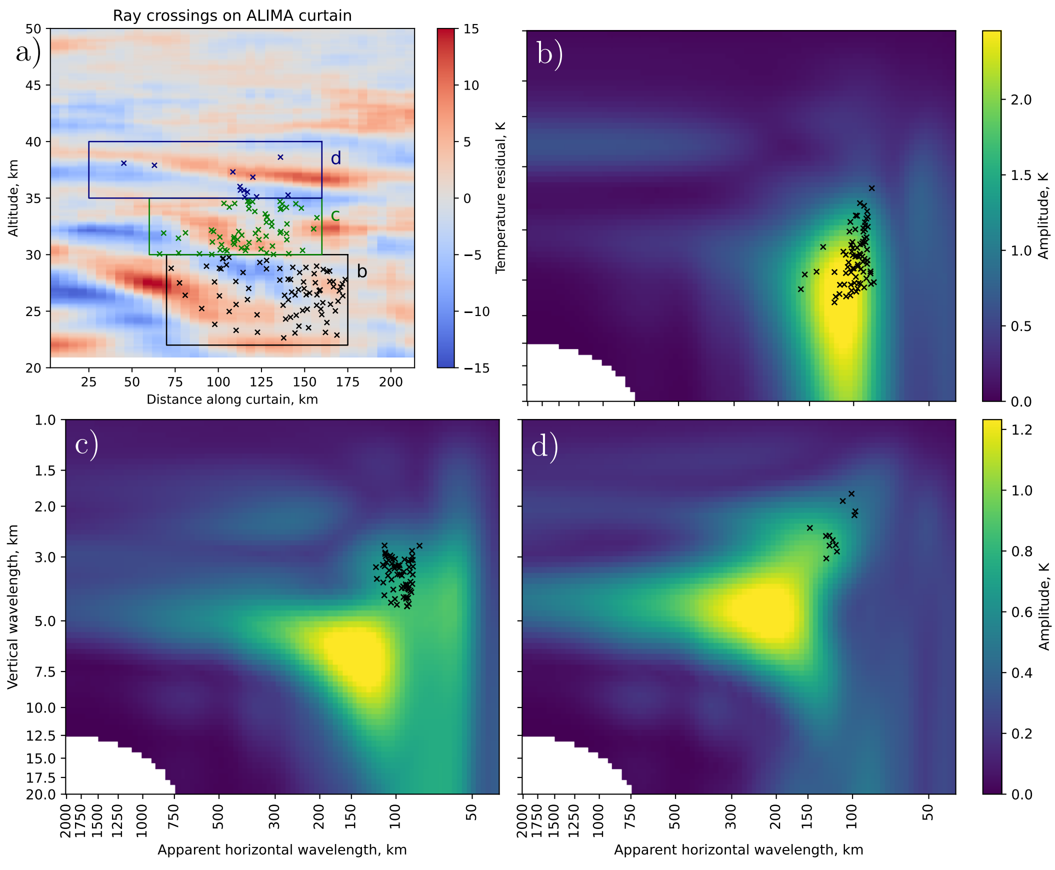

Figure 12. Similar to Figure 9, but shows GLORIA data-initialised GW rays crossing ALIMA observations over flight leg 14.

[5] Note that GLORIA data is limited to $\lambda_z < 10.5$ km, and GLORIA-initialized rays cover the majority of peak area satisfying this condition

3.4 Gravity Wave Propagation over the Andes

We will now compare our multi-instrument observations with model data and identify key processes that govern the most interesting aspects of the propagation of the observed GWs.

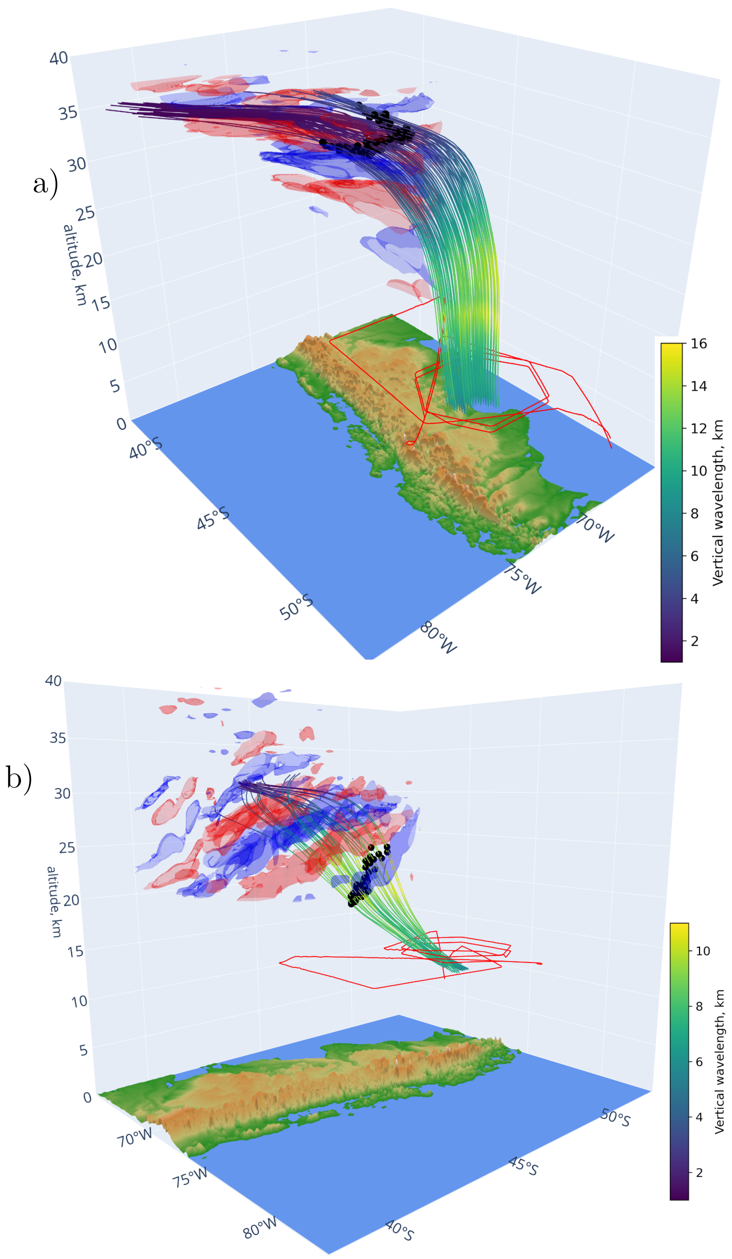

Figure 13. GLORIA-data-initialised GROGRAT rays (colored lines) are shown with ECMWF operational analysis temperature residuals (red and blue isosurfaces represent $\pm 4\,\mathrm{K}$ temperature residual, respectively) for 12:00 UTC. Black dots show wave packet positions along the ray at that time. Isosurfaces far from the rays not shown in order not to overload the plots. Panel a) shows short waves (ray groups e and f in Figure 9a), panel b) – long waves (groups c and d).

Figure 13a shows the ray traces of the the shorter-λ_h wave fits (ray groups e and f in Figure 9a) together with ECMWF operational analysis data valid approximately 6 h after observation. Waves propagate upwards quickly reaching the altitude of over 30 km in 6 h, and then turn NW. The volume occupied by the rays agrees well with the volume where ECMWF shows strong wave activity. Most importantly, the extent of wave activity over the Pacific is very similar for both rays and ECMWF-resolved waves at all altitudes. This clearly demonstrates that waves over Pacific at around 35 km altitude that were seen in ECMWF forecasts during the campaign and suspected to be non-orographic GWs (Section 3.1) are indeed mountain waves and originate from the Andes close to the location of the hexagonal flight pattern. The longer-λ_h waves (Figure 13b; showing ray groups c and d from Figure 9a) propagate more obliquely over the South American continent (where ECMWF shows a lot of waves as well) and break upon reaching a critical layer (also as predicted by ECMWF), which is lower in that region compared to the Pacific coast.

The main features of the ray paths can be understood from linear wave theory. The GW group velocity can be expressed as (e.g. Fritts & Alexander, 2003)

$$(c_{gx}, c_{gy}, c_{gz}) = (U, V, 0) + \frac{Nm}{\sqrt{k^2 + l^2}} \frac{\left(km, lm, -k^2 - l^2\right)}{\left(k^2 + l^2 + m^2\right)^{3/2}}, \tag{5}$$

where $\mathbf{k} = (k, l, m)$ and $\mathbf{U} = (U, V)$ are wave vector and horizontal background wind vector, respectively, in Cartesian coordinates. Since typically $\lambda_h \gg \lambda_z$, $m^2 \gg l^2 + k^2$, equation (5) implies $c_{gz} \approx N\sqrt{k^2 + l^2}/m^2$ is higher for waves with higher λ_z (lower $|m|$). This is one of the reasons why the waves of Figure 13a, with their relatively high λ_z, initially travel almost vertically and horizontal propagation only takes over near the critical layer, when λ_z decreases dramatically. The waves of Figure 13b have lower λ_z and propagate more obliquely from the start. They also reach much lower altitude during the first 6 h of propagation, as seen in Figure 13.

The horizontal direction of wave propagation is determined by several factors. In general, mountain waves tend to propagate along their horizontal phase lines, which mirrors the orientation of the mountain ridges (cf. e.g. Strube et al. (2021), Appendix A). This is because their ground-based horizontal phase velocity can be written as $\mathbf{c}_{gh} = \mathbf{U} + \hat{\mathbf{c}}_{gh}$, where $\hat{\mathbf{c}}_{gh}$ is the intrinsic horizontal group velocity, which is typically equal and opposite to the projection of the wind vector perpendicular to the mountain range (this results in a stationary wave-front pattern over the mountain). Therefore, the components of $\mathbf{c}_{gh}$ perpendicular to the mountain range cancel out, and $\mathbf{c}_{gh}$ is directed along the mountain range. Indeed Figure 13 shows rays initially pointing in the general northward direction, along the main Andes ridge.

The wave propagation direction can change due to horizontal refraction. Then due to horizontal wind gradients (k, l) turns (and hence $\hat{\mathbf{c}}_{gh}$, which is parallel to (k, l)). Horizontal refraction is expressed by the ray tracing equations (e.g. Marks & Eckermann, 1995)

$$\frac{dk}{dt} \approx -k\frac{\partial U}{\partial x} - l\frac{\partial V}{\partial x} \tag{6}$$

$$\frac{dl}{dt} \approx -k\frac{\partial U}{\partial y} - l\frac{\partial V}{\partial y} \tag{7}$$

where we have omitted some small terms by neglecting the horizontal gradient of N and the latitudinal gradient of the Coriolis parameter f. In this form, the equations do not have any terms related to the zonal and meridional directions specifically and are therefore valid for any local Cartesian coordinate system on a horizontal plane. Consider a wave packet with horizontal wave vector (k, l) and a "primed" Cartesian coordinate system (x', y') such that at with x' axis is parallel to (k, l). Then in the "primed" coordinate system $k' = \sqrt{k^2 + l^2}$, $l' = 0$, dk'/dt describes the change in horizontal wave vector magnitude, and dl'/dt describes the rotation of horizontal wave vector at the position of the wave packet. Equation (7)

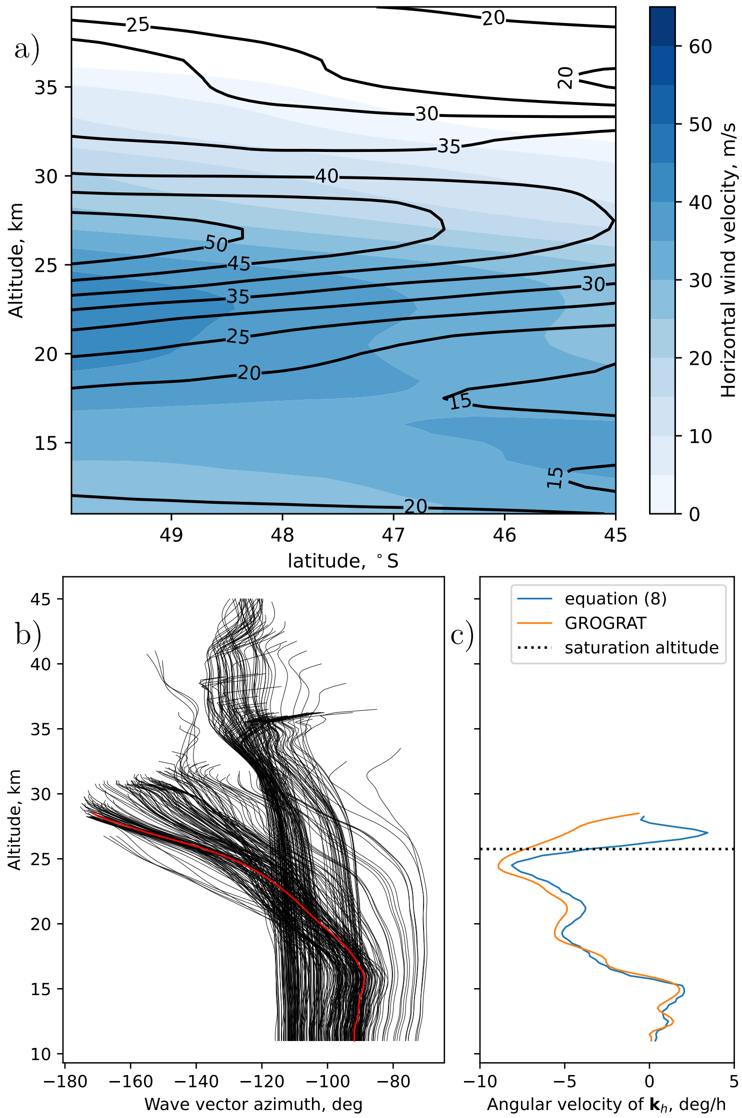

Figure 14. Panel a – horizontal winds on a vertical section through the center of the hexagonal flight pattern oriented in meridional direction. Color scale – zonal wind, contours – meridional wind. Panel b – direction of the wave vector, positive values clockwise from due N. Panel c – angular velocity of the horizontal wave vector for the ray highlighted in red in the Panel b, left. Orange line – as calculated by the ray tracer, blue line – simple estimate based on equation (9). Black dots mark the altitude where the ray reached saturation (just below critical level).

implies

$$\frac{dl'}{dt} = -k'\frac{\partial U'}{\partial y'}, \tag{8}$$

i.e. horizontal refraction occurs, if the wind component parallel to the wave vector has a gradient perpendicular to the wave vector. The angular velocity of rotation is

$$\frac{d\alpha}{dt} = \frac{1}{k'}\frac{dl'}{dt} = -\frac{\partial U'}{\partial y'} = -\frac{(-l,k)}{\sqrt{l^2+k^2}}\cdot\nabla\left(\frac{(U,V)\cdot(k,l)}{\sqrt{l^2+k^2}}\right) = \frac{l^2V_x - k^2U_y + lk(U_x - V_y)}{l^2+k^2}, \tag{9}$$

where $U_x = \partial U/\partial x$, etc.

The horizontal wind gradients that cause the refraction of the waves in our study are visible in Figure 14a, which presents the zonal and meridional winds on a vertical section going north from the center of the hexagonal flight pattern. Figure 14b shows the evolution of wave vector azimuth for the GLORIA-initialised GROGRAT rays as they propagated upwards. Very strong horizontal refraction is evident, with some rays turning by as much as 70°. This also explains why the waves over the Pacific had unexpected orientation (e.g. Figure 2b), causing speculation of non-orographic waves during flight planning. The ray-tracing predictions are confirmed by the ALIMA observations, as wrong wave orientation would inevitably result in wrong wavelengths on the ALIMA plane of observation. We took one strongly refracted ray (Figure 14c) as an example to demonstrate that our simplified framework to explain horizontal refraction with horizontal wind gradients (equations (6)–(9)) accounts for the majority of wind vector rotation predicted by the ray tracer. The agreement between the two methods becomes worse close to the critical level, as the terms neglected in equations (6)–(7) are no longer small when the wave attains very low group velocities.

Refraction of such strength is significant, as GWs carry horizontal momentum that is parallel to the wave vector. Turning of the vector implies momentum exchange between the waves and the background wind field, which can have significant impact on the winds (e.g. Buehler & McIntyre, 2003). The study presented in this paper is local by nature. GLORIA observations only cover a relatively small stretch of the Andes, and GWs observed by ALIMA at higher altitudes are clearly excited by GWs originating from mountains to the east of the Andes main ridge as well. Therefore, we cannot quantify the impact on the background flow just using the data presented here, but we can show that horizontal refraction plays a crucial role on whatever impact mountains waves can have on middle atmosphere dynamics.

Zonal and meridional GWMF for the GROGRAT rays used in this study is presented in Figure 15. One can see that horizontal refraction significantly alters GWMF. There are some waves that are excited with negligible meridional GWMF, refract significantly while propagating from 15 km to 25 km altitude and hence acquire a meridional GWMF value of the same order as their initial zonal GWMF, and deposit this momentum in the altitudes from 25 km to 30 km reaching their critical level. This clearly shows that horizontal refraction must be considered when studying the effects of GWs on the middle atmosphere circulation. Though effects of such wave direction changes were studied theoretically (Buehler & McIntyre, 2003) and in using models (Preusse et al., 2009), only the SouthTRAC campaign allowed to observe and quantify this effect in nature for a first time. The ECMWF-resolved waves further support these findings.

3.5 Mountain Wave Model Results and Model Comparison

The mountain wave model (MWM, see Section 2.5) is tested by modelling GWs observed during the measurement flight analysed in this paper and comparing the results to GLORIA and ALIMA data. Figure 16 compares actual GLORIA measurement to MWM simulation results with GLORIA observational filter applied. The observational filter is realised by generating synthetic GLORIA observations from MWM temperature data with the GLORIA radiance forward model and applying the same tomographic retrieval as for the real observations. One can see that the MWM captured the major features of the waves inside the hexagon, such as a high-amplitude wave almost parallel to the mountain ridges around the center of the hexagon and short waves in its eastern half. However, there are significant differences as well: MWM data has a strong positive temperature anomaly in the north of the hexagon which is not seen in the actual GLORIA data. Also, MWM data shows a group of waves with east-west wave front orientation on the western side of the hexagon that GLORIA did not observe. Within the MWM, these waves were excited over mountain ridges of east-west orientation deep inland in South America. It is possible that

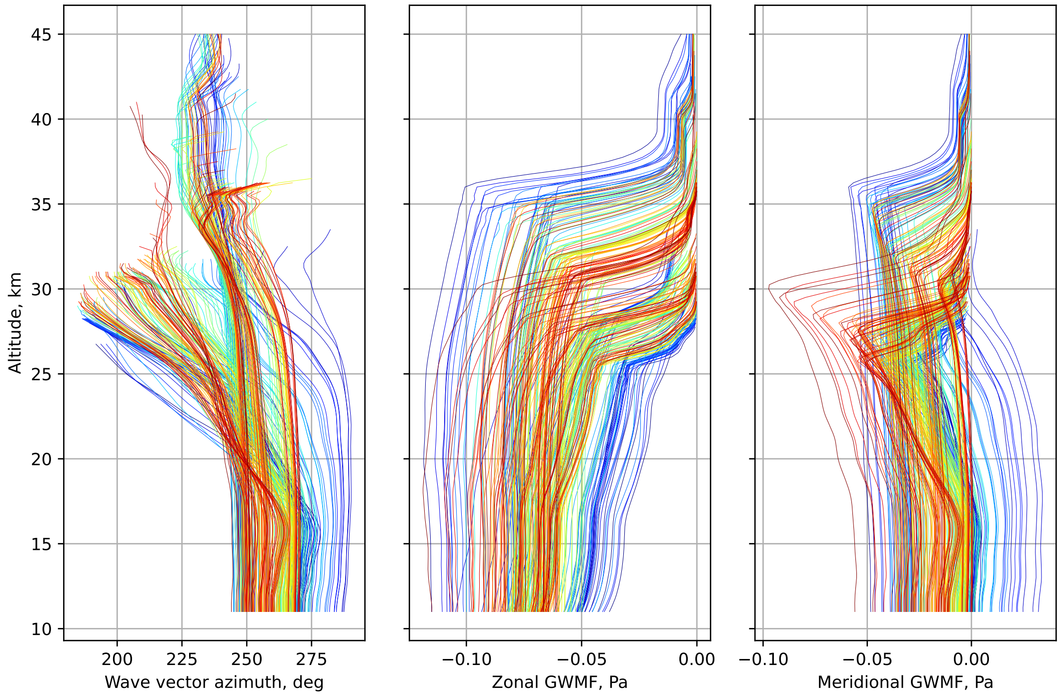

Figure 15. The evolution of wave vector azimuth and both components of the horizontal GWMF with altitude for each GROGRAT ray in our study.

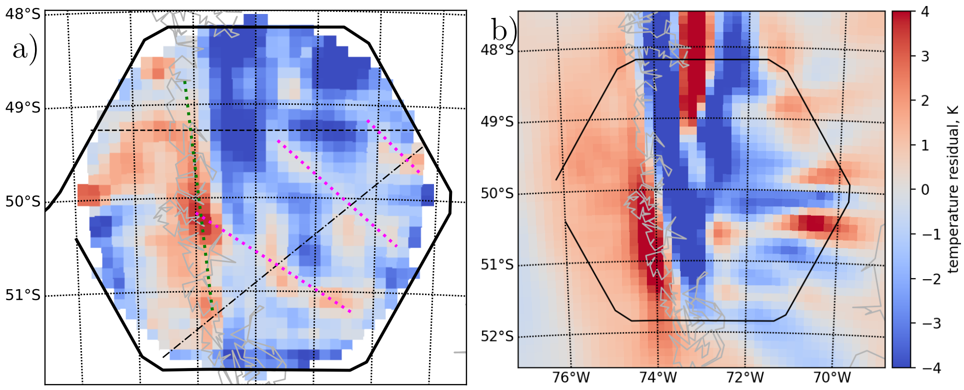

Figure 16. Panels show a horizontal cut at 12 km altitude through the GLORIA 3D tomography volume. Panel a) shows actual GLORIA data retrieved from the second hexagon (repeated from Figure 4), panel b) MWM data with GLORIA observational filter.

the actual wind over these ridges was weaker than the model expected due to blocking or complex wind interaction with the main part of the Andes.

Figure 17 shows a comparison of ALIMA observations from three flight legs with significant GW activity to MWM and ECMWF data. MWM seems to predict the strongest wave activity in correct locations, but the dominant wavelengths in MWM seem to be systematically shorter than seen in ALIMA data. It is possible that the longer waves, that are excited by wind interaction with large scale features (such as the whole mountain range) are not adequately represented in MWM. ECMWF data only has sufficient resolution to capture the longest waves in the ALIMA spectrum. These are represented well in most locations, but there are still some puzzling discrepancies, such as an almost complete lack of waves over the Pacific below around 35 km altitude (leg 3 and leg 5 after the 700 km mark). Also, even the highest amplitude, long wave that dominated flight leg 5 only has a low-amplitude extension over the Pacific. For these problematic areas, waves seem to be missing in MWM data as well. Observations are clearly still needed to improve model performance for mountain waves.

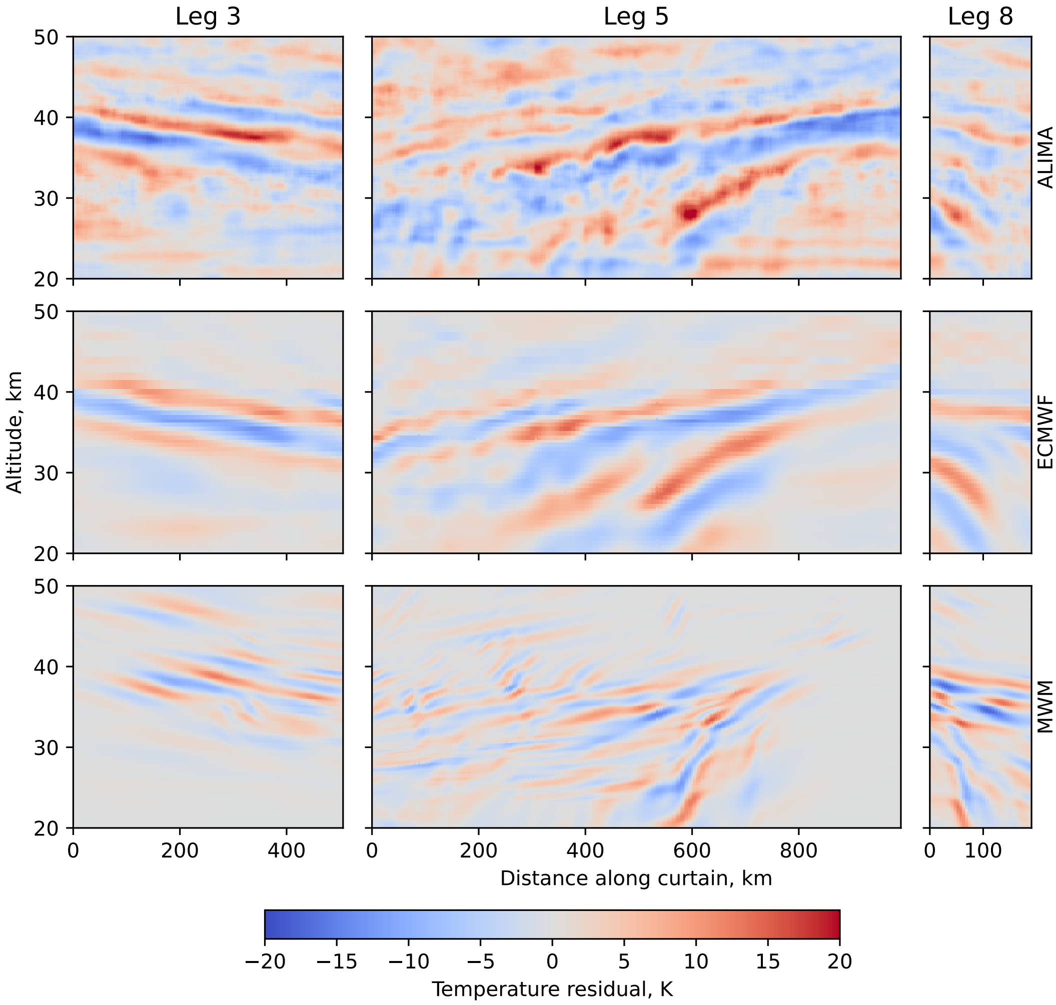

Figure 17. A comparison between ALIMA data, ECMWF operational analysis and mountain wave model simulations for flight legs 3, 5 and 8. Positions of each leg can be seen on the map in Figure 2a, marked L3, L5, L8, respectively.

4 Conclusions

The SouthTRAC aircraft measurement campaign was carried out in September-November 2019 with the German HALO research aircraft. Here we present the measurements by the GLORIA infrared limb imager and by the ALIMA lidar from a measurement flight on 20-21 September that observed a high amplitude mountain wave pattern over the Andes.

This flight included a hexagonal flight pattern around part of the Andes and the Pacific coast, which allowed us to perform a 3-D tomographic temperature retrieval within the hexagonal flight pattern at the altitude range from 8 km to 13 km. GLORIA is the only instrument capable to retrieve 3-D data of such detail in the UTLS region. The data revealed a complex gravity wave pattern that included a wide variety of wavelengths and different wave-front orientations. Gravity wave amplitudes and their full 3-D wave vectors were obtained from the GLORIA observations using small-volume least-squares fitting of sinusoidal plane waves. Since, according to linear theory, amplitudes and wave vectors fully describe a GW, we were able to use GLORIA data to initialise the GROGRAT ray tracer. Ray tracing results confirmed that the observed waves were excited over the Andes and propagated obliquely. The ray-tracer also allows to predict wave propagation after the measurement. Most of these GLORIA-initialised rays propagated through the atmospheric regions observed by the ALIMA lidar, allowing to compare the data sets provided by the two instruments. Very good agreement was found: the wavelengths of GLORIA rays, as they were crossing the volumes with ALIMA observations, matched the spectral peaks of ALIMA data everywhere except for the cases with very long ray travel times (i.e. when the GLORIA-initialised rays arrived at the location of the ALIMA observations more than about 12 h after the measurement). Also, every major peak in the ALIMA spectrum had corresponding GLORIA-initialised rays. These rays could be back-traced to orography, which strongly suggests that the wave pattern observed by both GLORIA and ALIMA could be explained by mountain wave activity, at least to a large extent. These results serve as a validation for our least-squares wave-fitting technique (S3D) and ray tracing code (GROGRAT).

Rays initialized from GLORIA data generally occupied the same volumes where ECMWF operational analyses showed enhanced wave activity. There was one wave pattern in ECMWF data (present both in operational analysis and in forecast data available before the flight) that was of particular interest: at altitudes of around 30 km wave activity was strong over the ocean west of the Andes main ridge and thus seemingly upstream of the Andes. These GWs did not appear to be of orographic origin due to their position and wave front orientation. We showed, based on both GLORIA and ALIMA data, that these waves did indeed originate from the Andes, but had been excited south of their observed location, had experienced strong horizontal refraction and propagated along their phase fronts towards the west of the main ridge. The ECMWF-IFS in its configuration of 2019 resolves waves with wavelength longer than 100 km. Compared to ALIMA observations, the ECMWF data captured most of these meso-scale waves well, but there are some notable differences between model and observations. For example, ECMWF had significantly lower GW amplitudes in the part of the wave pattern that extended over the Pacific. The same difference was found for the MWM, which also underestimated this part of the wave field. The main features of GLORIA and ALIMA observations were predicted by the MWM, but the model tended to underestimate vertical wavelengths in the stratosphere and overestimate the amplitudes of waves excited by wind flow over minor ridges.

The combination of GLORIA and ALIMA data allowed to obtain direct experimental evidence on horizontal refraction by comparing the horizontal wavelengths of the GLORIA-initialized rays and the horizontal wavelengths from ALIMA. This phenomenon had never been directly observed before the SouthTRAC campaign. In our case study, horizontal refraction played a major part in shaping the overall wave structure and the interaction with the background flow. Most of the waves were excited with wave-fronts parallel to the main mountain ridge as confirmed by the GLORIA observations. At larger altitudes, however, the waves had turned by about 45° and wave vectors pointed to the south-east. Due to this turn of the wave vector, and the nature of the wind profile, the bulk of the waves moved from the center of the hexagon to the North and East, i.e. the ground-based wave group velocity was oriented meridionally rather than zonally, which amounts to significant meridional transport of zonal momentum. The current GCMs inability to adequately represent this process contributes to the problem of the missing GW drag at 60°S. Also, most of the observed waves carried almost no meridional momentum at the time they were excited at the Andes, but some acquired so much meridional momentum due to horizontal refraction, that they deposited more meridional than zonal momentum at the critical layer. This demonstrates that current parametrizations with only vertical propagation and no refraction neglect important features of the wave driving both in terms of location and direction of the exerted drag. Therefore, the effect such waves have on the general circulation cannot be adequately represented without more detailed representations of gravity waves in general circulation models. Further development of the models should be constrained by high-resolution observations. Our results also suggest that, at least in the presence of horizontal wind shear, significant momentum exchange between gravity waves and the background flow can occur without wave breaking, which is often overlooked while identifying regions where gravity wave drag can occur. The current case can provide such a ground truth, but global data would be required to quantify the effect on the global circulation. Observations similar to the ones presented here could be performed for all regions of the Earth and on a regular basis by bringing an infrared limb sounder into space. GLORIA demonstrates that the technique is mature and provides data of high quality.

Open Research

GLORIA, ALIMA and BAHAMAS data from the SouthTRAC measurement campaign is available after registration through the HALO database (HALO database, 2022) of the German Aerospace agency (Deutsches Zentrum für Luft- und Raumfahrt, DLR). The relevant data sets for the measurement flight of 20-21 September 2019 (SouthTRAC flight 12, ST12), on which this work is based, are as follows: GLORIA (*HALO database: GLORIA ST12*, 2021), ALIMA (*HALO database: ALIMA ST12*, 2021), BAHAMAS (*HALO database: BAHAMAS ST12*, 2019).

ECMWF operational analysis data is available after registration from ECMWF (*ECMWF operational analysis*, 2022).

Acknowledgments

The authors gratefully acknowledge the computing time granted through JARA on the supercomputer JURECA at Forschungszentrum Jülich. The European Centre for Medium-Range Weather Forecasts (ECMWF) is acknowledged for meteorological data support. The authors especially thank the GLORIA team, including the institutes ZEA-1, ZEA-2 at Forschungszentrum Jülich and the institute for Data Processing and Electronics at the Karlsruhe Institute of Technology, for their great work during the SouthTRAC campaign on which all the data in this paper are based. We would also like to thank the SouthTRAC flight planning team as well as the pilots and the ground support team at the Flight Experiments facility of the Deutsches Zentrum für Luft- und Raumfahrt (DLR-FX).

The SouthTRAC measurement campaign was supported by the German Science Foundation (Deutsche Forschungsgemeinschaft,DFG) under the Priority Program SPP 1294. This work was also supported by the DFG project number 423229691 (grant no. HALO-SPP 1294/PR 919/5-1), and Federal Ministry of Education and Research of Germany (BMBF) research initiative Role of the Middle Atmosphere in Climate (ROMIC), project WASCLIM. Wolfgang Woiwode is supported by BMBF ROMIC, project WASCLIM, subproject 5, grant 01LG1907E.

References

Alexander, M. J., & Barnet, C. D. (2007). Using satellite observations to constrain gravity wave parameterizations for global models. *J. Atmos. Sci.*, *64*(5), 1652-1665.

Alexander, M. J., & Dunkerton, T. J. (1999). A spectral parameterization of mean-flow forcing due to breaking gravity waves. *J. Atmos. Sci.*, *56*, 4167-4182.

Alexander, M. J., & Rosenlof, K. H. (2003). Gravity-wave forcing in the stratosphere: Observational constraints from the upper atmosphere research satellite and implications for parameterization in global models. *J. Geophys. Res.*, *108*(D19), 4597. doi:

10.1029/2003JD003373

Amante, C., & Eakins, B. (2009). *Etopo1 1 arc-minute global relief model: Procedures, data sources and analysis.* National Centers for Environmental Information, NESDIS, NOAA, U.S. Department of Commerce. (last access: 20 February 2020) doi: 10.7289/V5C8276M

Andrews, D. G., Holton, J. R., & Leovy, C. B. (1987). *Middle atmosphere dynamics* (Vol. 40). Academic Press.

Bacmeister, J., Newman, P., Gary, B., & Chan, K. (1994, JUN). An algorithm for forecasting mountain wave-related turbulence in the stratosphere. *Wea. Forecast.*, *9*(2), 241-253. doi: 10.1175/1520-0434(1994)009⟨0241:AAFFMW⟩2.0.CO;2

Bacmeister, J. T. (1993). Mountain-wave drag in the stratosphere and mesosphere inferred from observed winds and a simple mountain-wave parameterization scheme. *J. Atmos. Sci.*, *50*, 377-399.

Buehler, O., & McIntyre, M. E. (2003). Remote recoil: a new wave-mean interaction effect. *J. Fluid Mech.*, *492*, 207-230.

Bühler, O. (1999). On shear-generated gravity waves that reach the mesosphere. part i: Wave generation. *J. Atmos. Sci.*, *56*, 3749-3773.

Butchart, N., Charlton-Perez, A. J., Cionni, I., Hardiman, S. C., Haynes, P. H., Krueger, K., ... Yamashita, Y. (2011, MAR 3). Multimodel climate and variability of the stratosphere. *J. Geophys. Res. Atmos.*, *116*. doi: 10.1029/2010JD014995

(C3S), C. C. C. S. (2017). *Era5: Fifth generation of ecmwf atmospheric reanalyses of the global climate.* Copernicus Climate Change Service Climate Data Store (CDS). Retrieved from `https://cds.climate.copernicus.eu/cdsapp#!/home`

Cao, B., Heale, C. J., Guo, Y., Liu, A. Z., & Snively, J. B. (2016). Observation and modeling of gravity wave propagation through reflection and critical layers above andes lidar observatory at cerro pachón, chile. *J. Geophys. Res. Atmos.*, *121*(21), 12,737–12,750. Retrieved from `http://dx.doi.org/10.1002/2016JD025173` (2016JD025173) doi: 10.1002/2016JD025173

Center, N. N. G. D. (2009). *ETOPO1 1 arc-minute global relief model.* NOAA National Centers for Environmental Information. Retrieved from `https://www.ngdc.noaa.gov/mgg/global/` (last access: 19 May 2022)

Charron, M., & Manzini, E. (2002). Gravity waves from fronts: Parameterization and middle atmosphere response in a general circulation model. *J. Atmos. Sci.*, *59*, 923-941.

Chen, C.-C., Durran, D. R., & Hakim, G. J. (2005). Mountain-wave momentum flux in an evolving synoptic-scale flow. *J. Atmos. Sci.*, *62*(9), 3213 - 3231. doi: 10.1175/JAS3543.1

Choi, H.-J., Chun, H.-Y., & Song, I.-S. (2009, APR 24). Gravity wave temperature variance calculated using the ray-based spectral parameterization of convective gravity waves and its comparison with Microwave Limb Sounder observations. *J. Geophys. Res.*, *114*. doi: 10.1029/2008JD011330

Curtis, A. R. (1952). Discussion of 'A statistical model for water vapour absorption' by R. M. Goody. *Quart. J. Roy. Meteorol. Soc.*, *78*, 638-640.

Dee, D. P., Uppala, S. M., Simmons, A. J., Berrisford, P., Poli, P., Kobayashi, S., ... Vitart, F. (2011). The era-interim reanalysis: configuration and performance of the data assimilation system. *Quart. J. Roy. Meteorol. Soc.*, *137*(656), 553-597. doi: 10.1002/qj.828

de Groot-Hedlin, C. D., Hedlin, M. A. H., Hoffmann, L., Alexander, M. J., & Stephan, C. C. (2017, NOV 16). Relationships between gravity waves observed at Earth's surface and in the stratosphere over the central and eastern United States. *J. Geophys. Res. Atmos.*, *122*(21), 11482-11498. doi: 10.1002/2017JD027159

de la Camara, A., Lott, F., & Hertzog, A. (2014, NOV 16). Intermittency in a stochastic parameterization of nonorographic gravity waves. *J. Geophys. Res. Atmos.*, *119*(21), 11905-11919. doi: 10.1002/2014JD022002

de la Torre, A., Hierro, R., Llamedo, P., & Alexander, P. (2011). Severe hailstorms near Southern Andes in the presence of mountain waves. *Atmos. Res.*, 112-123. doi: 10

.1016/j.atmosres.2011.01.015
Dunkerton, T. J. (1997). Shear instability of internal inertia-gravity waves. *J. Atmos. Sci.*, *54*, 1628-1641.
Eckermann, S. D., & Preusse, P. (1999). Global measurements of stratospheric mountain waves from space. *Science*, *286*(5444), 1534-1537. doi: 10.1126/science.286.5444.1534
ECMWF operational analysis. (2022). https://www.ecmwf.int/en/forecasts/datasets. (last access: 4 September 2022)
Einaudi, F., & Hines, C. O. (1970). WKB approximation in application to acoustic–gravity waves. *Can. J. Phys.*, *48*(12), 1458–1471. doi: 10.1139/p70-185
Ern, M., Hoffmann, L., & Preusse, P. (2017, JAN). Directional gravity wave momentum fluxes in the stratosphere derived from high-resolution AIRS temperature data. *Geophys. Res. Lett.*, *44*(1), 475-485. doi: 10.1002/2016GL072007
Ern, M., Hoffmann, L., Rhode, S., & Preusse, P. (2022). The mesoscale gravity wave response to the 2022 Tonga volcanic eruption: AIRS and MLS satellite observations and source backtracing. *Geophys. Res. Lett.*. doi: 10.1029/2022GL098626
Ern, M., Ploeger, F., Preusse, P., Gille, J. C., Gray, L. J., Kalisch, S., … Riese, M. (2014). Interaction of gravity waves with the QBO: A satellite perspective. *J. Geophys. Res. Atmos.*, *119*, 2329-2355. doi: 10.1002/2013JD020731
Ern, M., Preusse, P., & Riese, M. (2015). Driving of the SAO by gravity waves as observed from satellite. *Ann. Geophys.*, *33*(4), 483-504. doi: 10.5194/angeo-33-483-2015
Ern, M., Preusse, P., & Warner, C. D. (2006). Some experimental constraints for spectral parameters used in the Warner and McIntyre gravity wave parameterization scheme. *Atmos. Chem. Phys.*, *6*(12), 4361-4381. doi: 10.5194/acp-6-4361-2006
Ern, M., Trinh, Q. T., Kaufmann, M., Krisch, I., Preusse, P., Ungermann, J., … Riese, M. (2016, AUG 9). Satellite observations of middle atmosphere gravity wave absolute momentum flux and of its vertical gradient during recent stratospheric warmings. *Atmos. Chem. Phys.*, *16*(15), 9983-10019. doi: 10.5194/acp-16-9983-2016
Ern, M., Trinh, Q. T., Preusse, P., Gille, J. C., Mlynczak, M. G., Russell III, J. M., & Riese, M. (2018). GRACILE: A comprehensive climatology of atmospheric gravity wave parameters based on satellite limb soundings. *Earth Syst. Sci. Dat.*, *10*, 857-892. Retrieved from https://www.earth-syst-sci-data.net/10/857/2018/ doi: 10.5194/essd-10-857-2018
Fovell, R., Durran, D., & Holton, J. R. (1992). Numerical simulations of convectively generated stratospheric gravity waves. *J. Atmos. Sci.*, *49*, 1427-1442.
Friedl-Vallon, F., Gulde, T., Hase, F., Kleinert, A., Kulessa, T., Maucher, G., … Ungermann, J. (2014). Instrument concept of the imaging Fourier transform spectrometer GLORIA. *Atmos. Meas. Tech.*, *7*(10), 3565-3577. doi: 10.5194/amt-7-3565-2014
Fritts, D., & Alexander, M. (2003, APR 16). Gravity wave dynamics and effects in the middle atmosphere. *Rev. Geophys.*, *41*(1). doi: 10.1029/2001RG000106
Garcia, R. R., Marsh, D., Kinnison, D. E., Boville, B., & Sassi, F. (2007). Simulations of secular trends in the middle atmosphere 1950-2003. *J. Geophys. Res.*, *112*, D09301. doi: 10.1029/2006JD007485
Garcia, R. R., Smith, A. K., Kinnison, D. E., de la Camara, A., & Murphy, D. J. (2017). Modification of the gravity wave parameterization in the whole atmosphere community climate model: Motivation and results. *J. Atmos. Sci.*, *74*(1), 275-291. doi: 10.1175/JAS-D-16-0104.1
Garcia, R. R., & Solomon, S. (1985). The effect of breaking gravity waves on the dynamics and chemical composition of the mesosphere and lower thermosphere. *J. Geophys. Res.*, *90*, 3850-3868.
Geldenhuys, M., Kaifler, B., Preusse, P., Ungermann, J., Alexander, P., Krasauskas, L., … et al. (2022). Observations of gravity wave refraction and its causes and consequences. *Earth and Space Science Open Archive*, 36. Retrieved from https://doi.org/10.1002/essoar.10511036.1 doi: 10.1002/essoar.10511036.1
Geldenhuys, M., Preusse, P., Krisch, I., Zülicke, C., Ungermann, J., Ern, M., … Riese, M. (2021). Orographically induced spontaneous imbalance within the jet causing a

large-scale gravity wave event. *Atmos. Chem. Phys.*. doi: 10.5194/acp-21-10393-2021

Gille, J. C., Barnett, J. J., Whitney, J. G., Dials, M. A., Woodard, D., Rudolf, W. P., ... Mankin, W. (2003). The High-Resolution Dynamics Limb Sounder (HIRDLS) experiment on AURA. *Proc. SPIE*, *5152*, 161-171. doi: 10.1117/12.507657

Godson, W. L. (1953). The evaluation of infra-red radiative fluxes due to atmospheric water vapour. *Quart. J. Roy. Meteorol. Soc.*, *79*, 367-379.

Gordley, L. L., & Russell, J. M. (1981). Rapid inversion of limb radiance data using an emissivity growth approximation. *Appl. Optics*, *20*, 807-813. doi: 10.1364/AO.20.000807

HALO database. (2022). Retrieved from `https://halo-db.pa.op.dlr.de/` (last access: 04 September 2022) doi: 10.17616/R39Q0T

HALO database: ALIMA ST12. (2021). `https://halo-db.pa.op.dlr.de/dataset/7516`. (revision 3, last access: 4 September 2022)

HALO database: BAHAMAS ST12. (2019). `https://halo-db.pa.op.dlr.de/dataset/6482`. (revision 1, last access: 4 September 2022)

HALO database: GLORIA ST12. (2021). `https://halo-db.pa.op.dlr.de/dataset/6803`. (revision 5, last access: 4 September 2022)

Hasha, A., Bühler, O., & Scinocca, J. (2008). Gravity wave refraction by three-dimensionally varying winds and the global transport of angular momentum. *J. Atmos. Sci.*, *65*, 2892-2906.

Hersbach, H., Bell, B., Berrisford, P., Biavati, G., Horányi, A., Muñoz Sabater, J., ... Thpaut, J.-N. (2018). *Era5 hourly data on pressure levels from 1979 to present.* Copernicus Climate Change Service (C3S) Climate Data Store (CDS). doi: 10.24381/cds.bd0915c6

Hertzog, A., Boccara, G., Vincent, R. A., Vial, F., & Cocquerez, P. (2008). Estimation of gravity wave momentum flux and phase speeds from quasi-Lagrangian stratospheric balloon flights. part ii: Results from the vorcore campaign in antarctica. *J. Atmos. Sci.*, *65*(10), 3056-3070. doi: 10.1175/2008JAS2710.1

Hestenes, M. R., & Stiefel, E. (1952). Methods of conjugate gradients for solving linear systems. *J Res NIST*, *49*(6), 409–436. doi: 10.6028/jres.049.044

Hindley, N. P., Wright, C. J., Hoffmann, L., Moffat-Griffin, T., & Mitchell, N. J. (2020, NOV 28). An 18-year climatology of directional stratospheric gravity wave momentum flux from 3-D satellite observations. *Geophys. Res. Lett.*, *47*(22), e2020GL089557. doi: 10.1029/2020GL089557

Hindley, N. P., Wright, C. J., Smith, N. D., & Mitchell, N. J. (2015). The southern stratospheric gravity wave hot spot: individual waves and their momentum fluxes measured by COSMIC GPS-RO. *Atmos. Chem. Phys.*, *15*(14), 7797-7818. doi: 10.5194/acp-15-7797-2015

Hoffmann, L., Grimsdell, A. W., & Alexander, M. J. (2016). Stratospheric gravity waves at southern hemisphere orographic hotspots: 2003–2014 airs/aqua observations. *Atmos. Chem. Phys.*, *16*(14), 9381–9397.

Hoffmann, L., Kaufmann, M., Spang, R., Müller, R., Remedios, J. J., Moore, D. P., ... Riese, M. (2008). Envisat MIPAS measurements of CFC-11: retrieval, validation, and climatology. *Atmos. Chem. Phys.*, *8*, 3671-3688. doi: 10.1016/j.asr.2005.03.112

Holton, J. R. (2004). *An introduction to dynamic meteorology.* Academic Press Limited. (3rd edition)

Holton, J. R., & Alexander, M. J. (2000). The role of waves in the stransport circulation of the middle atmosphere. *American Geophysical Union*, *123*. (Washington DC)

Jiang, J., Wang, B., Goya, K., Hocke, K., Eckermann, S., Ma, J., ... Read, W. (2004, FEB 13). Geographical distribution and interseasonal variability of tropical deep convection: UARS MLS observations and analyses. *J. Geophys. Res. Atmos.*, *109*(D3). doi: 10.1029/2003JD003756

Kaifler, B., & Kaifler, N. (2021). A compact rayleigh autonomous lidar (coral) for the middle atmosphere. *Atmospheric Measurement Techniques*, *14*(2), 1715–1732. Retrieved from `https://amt.copernicus.org/articles/14/1715/2021/` doi: 10.5194/amt

-14-1715-2021

Kalisch, S., Preusse, P., Ern, M., Eckermann, S. D., & Riese, M. (2014). Differences in gravity wave drag between realistic oblique and assumed vertical propagation. *J. Geophys. Res. Atmos.*, *119*, 10,081-10,099. doi: 10.1002/2014JD021779

Kidston, J., Scaife, A. A., Hardiman, S. C., Mitchell, D. M., Butchart, N., Baldwin, M. P., & Gray, L. J. (2015). Stratospheric influence on tropospheric jet streams, storm tracks and surface weather. *Nature Geosci.*, *8*, 433-440. doi: 10.1038/ngeo2424

Kim, Y. H., Bushell, A. C., Jackson, D. R., & Chun, H.-Y. (2013, MAY 16). Impacts of introducing a convective gravity-wave parameterization upon the QBO in the met office unified model. *Geophys. Res. Lett.*, *40*(9), 1873-1877. doi: 10.1002/grl.50353

Kim, Y.-J., Eckermann, S. D., & Chun, H.-Y. (2003). An overview of the past, present and future of gravity-wave drag parameterization for numerical climate and weather prediction models. *Atmosphere-Ocean*, *41*, 65-98.

Koch, S. E., & Siedlarz, L. M. (1999). Mesoscale gravity waves and their environment in the central united states during storm-fest. *Mon. Weath. Rev.*, *127*, 2854-2879.

Krasauskas, L., Ungermann, J., Ensmann, S., Krisch, I., Kretschmer, E., Preusse, P., & Riese, M. (2019). 3-d tomographic limb sounder retrieval techniques: irregular grids and laplacian regularisation. *Atmos. Meas. Tech.*, *12*(2), 853–872. Retrieved from `https://www.atmos-meas-tech.net/12/853/2019/` doi: 10.5194/amt-12-853-2019

Krasauskas, L., Ungermann, J., Preusse, P., Friedl-Vallon, F., Zahn, A., Ziereis, H., ... Riese, M. (2021). 3-d tomographic observations of rossby wave breaking over the north atlantic during the wise aircraft campaign in 2017. *Atmos. Chem. Phys.*, *21*(13), 10249–10272. doi: 10.5194/acp-21-10249-2021

Krisch, I., Ern, M., Hoffmann, L., Preusse, P., Strube, C., Ungermann, J., ... Riese, M. (2020). Superposition of gravity waves with different propagation characteristics observed by airborne and space-borne infrared sounders. *Atmos. Chem. Phys.*, *20*(19), 11469–11490. Retrieved from `https://acp.copernicus.org/articles/20/11469/2020/` doi: 10.5194/acp-20-11469-2020

Krisch, I., Preusse, P., Ungermann, J., Dörnbrack, A., Eckermann, S. D., Ern, M., ... Riese, M. (2017). First tomographic observations of gravity waves by the infrared limb imager GLORIA. *Atmos. Chem. Phys.*, *17*(24), 14937–14953. doi: 10.5194/acp-17-14937-2017

Krisch, I., Ungermann, J., Preusse, P., Kretschmer, E., & Riese, M. (2018). Limited angle tomography of mesoscale gravity waves by the infrared limb-sounder GLORIA. *Atmos. Meas. Tech.*, *11*(7), 4327–4344. Retrieved from `https://www.atmos-meas-tech.net/11/4327/2018/` doi: 10.5194/amt-11-4327-2018

Lehmann, C. I., Kim, Y.-H., Preusse, P., Chun, H.-Y., Ern, M., & Kim, S.-Y. (2012). Consistency between fourier transform and small-volume few-wave decomposition for spectral and spatial variability of gravity waves above a typhoon. *Atmos. Meas. Tech.*, *5*(7), 1637-1651. doi: 10.5194/amt-5-1637-2012

Lighthill, M. J. (1978). Waves in fluids. *Cambridge University Press*, 504pp.

Lott, F., & Miller, M. J. (1997). A new subgrid scale orographic drag parameterization: Its formulation and testing. *Quart. J. Roy. Meteorol. Soc.*, *123*, 101-127.

Lu, X., Chen, C., Huang, W., Smith, J. A., Chu, X., Yuan, T., ... Cullens, C. Y. (2015). A coordinated study of 1 h mesoscale gravity waves propagating from logan to boulder with crrl na doppler lidars and temperature mapper. *J. Geophys. Res. Atmos.*, *120*(19), 10,006–10,021. Retrieved from `http://dx.doi.org/10.1002/2015JD023604` (2015JD023604) doi: 10.1002/2015JD023604

Marks, C. J., & Eckermann, S. D. (1995). A three-dimensional nonhydrostatic ray-tracing model for gravity waves: Formulation and preliminary results for the middle atmosphere. *J. Atmos. Sci.*, *52*(11), 1959-1984. doi: 10.1175/1520-0469(1995)052⟨1959:ATDNRT⟩2.0.CO;2

Marquardt, D. W. (1963). An algorithm for least-squares estimation of nonlinear parameters. *J. Soc. Ind. Appl. Math.*, *11*, 431-441.

McLandress, C. (1998). On the importance of gravity waves in the middle atmosphere and their parameterization in general circulation models. *J. Atm. Sol.-Terr. Phys.*, *60*, 1357-1383. doi: 10.1016/S1364-6826(98)00061-3

McLandress, C., Shepherd, T. G., Polavarapu, S., & Beagley, S. R. (2012, MAR). Is Missing Orographic Gravity Wave Drag near 60 degrees S the Cause of the Stratospheric Zonal Wind Biases in Chemistry Climate Models? *J. Atmos. Sci.*, *69*(3), 802-818. doi: 10.1175/JAS-D-11-0159.1

Minamihara, Y., Sato, K., & Tsutsumi, M. (2020). Intermittency of gravity waves in the antarctic troposphere and lower stratosphere revealed by the pansy radar observation. *Journal of Geophysical Research: Atmospheres*, *125*(15), e2020JD032543. doi: https://doi.org/10.1029/2020JD032543

Morlet, J., Arens, G., Fourgeau, E., & Glard, D. (1982). Wave propagation and sampling theory—part i: Complex signal and scattering in multilayered media. *GEOPHYSICS*, *47*(2), 203–221. doi: 10.1190/1.1441328

Nastrom, G., Fritts, D., & Gage, K. (1987, OCT 15). An investigation of terrain effects on the mesoscale spectrum of atmospheric motions. *J. Atmos. Sci.*, *44*(20), 3087-3096. doi: {10.1175/1520-0469(1987)044⟨3087:AIOTEO⟩2.0.CO;2}

Niekerk, A., & Vosper, S. (2021). Towards a more “scale-aware” orographic gravity wave drag parametrization: Description and initial testing. *Quart. J. Roy. Meteorol. Soc.*, *147*(739), 3243–3262. doi: 10.1002/qj.4126

O’Sullivan, D., & Dunkerton, T. J. (1995). Generation of inertia-gravity waves in a simulated life cycle of baroclinic instability. *J. Atmos. Sci.*, *52*(21), 3695-3716. doi: {10.1175/1520-0469(1995)052⟨3695:GOIWIA⟩2.0.CO;2}

Palmer, T. N., Shutts, G. J., & Swinbank, R. (1986). Alleviation of a systematic weterly bias in general circulation and numerical weather prediction models trough an orographic gravity wave drag parameterization. *Quart. J. Roy. Meteorol. Soc.*, *112*, 1001-1093.

Perrett, J. A., Wright, C. J., Hindley, N. P., Hoffmann, L., Mitchell, N. J., Preusse, P., . . . Eckermann, S. D. (2021, JAN 28). Determining gravity wave sources and propagation in the southern hemisphere by ray-tracing AIRS measurements. *Geophys. Res. Lett.*, *48*(2), e2020GL088621. doi: 10.1029/2020GL088621

Plougonven, R., de la Camara, A., Hertzog, A., & Lott, F. (2020, APR). How does knowledge of atmospheric gravity waves guide their parameterizations? *Quart. J. Roy. Meteorol. Soc.*, *146*(728, A), 1529-1543. doi: 10.1002/qj.3732

Plougonven, R., & Zhang, F. (2014, MAR). Internal gravity waves from atmospheric jets and fronts. *Rev. Geophys.*, *52*(1), 33-76. doi: 10.1002/2012RG000419

Podglajen, A., Hertzog, A., Plougonven, R., & Legras, B. (2016, April). Lagrangian temperature and vertical velocity fluctuations due to gravity waves in the lower stratosphere. *Geophys. Res. Lett.*, *43*, 3543-3553. doi: 10.1002/2016GL068148

Polichtchouk, I., Shepherd, T. G., Hogan, R. J., & Bechtold, P. (2018, MAY). Sensitivity of the Brewer-Dobson Circulation and Polar Vortex Variability to Parameterized Nonorographic Gravity Wave Drag in a High-Resolution Atmospheric Model. *J. Atmos. Sci.*, *75*(5), 1525-1543. doi: 10.1175/JAS-D-17-0304.1

Pramitha, M., Venkat Ratnam, M., Taori, A., Krishna Murthy, B. V., Pallamraju, D., & Vijaya Bhaskar Rao, S. (2015). Evidence for tropospheric wind shear excitation of high-phase-speed gravity waves reaching the mesosphere using the ray-tracing technique. *Atmos. Chem. Phys.*, *15*, 2709-2721. doi: 10.5194/acp-15-2709-2015

Preusse, P., Eckermann, S. D., Ern, M., Oberheide, J., Picard, R. H., Roble, R. G., . . . Mlynczak, M. G. (2009). Global ray tracing simulations of the SABER gravity wave climatology. *J. Geophys. Res. Atmos.*, *114*. doi: 10.1029/2008JD011214

Preusse, P., Hoffmann, L., Lehmann, C., Alexander, M. J., Broutman, D., Chun, H.-Y., . . . Vial, F. (2012). Observation of gravity waves from space. *Final report, ESA study, CN/22561/09/NL/AF*, pp 195.

Ralph, F., Neiman, P., & Keller, T. (1999). Deep-tropospheric gravity waves created by leeside cold fronts. *J. Atmos. Sci.*, *56*, 2986-3009. doi: 10.1175/1520-0469(1999)056⟨2986:DTGWCB⟩2.0.CO;2

Rao, J., Garfinkel, C. I., White, I. P., & Schwartz, C. (2020). The southern hemisphere minor sudden stratospheric warming in september 2019 and its predictions in s2s models. *Journal of Geophysical Research: Atmospheres*, *125*(14), e2020JD032723. (e2020JD032723 2020JD032723) doi: https://doi.org/10.1029/2020JD032723

Rapp, M., Kaifler, B., Dörnbrack, A., Gisinger, S., Mixa, T., Reichert, R., . . . Engel, A. (2020). Southtrac-gw: An airborne field campaign to explore gravity wave dynamics at the world's strongest hotspot. *Bulletin of the American Meteorological Society*. (submitted)

Riese, M., Friedl-Vallon, F., Spang, R., Preusse, P., Schiller, C., Hoffmann, L., . . . Höpfner, M. (2005). GLObal limb Radiance Imager for the Atmosphere (GLORIA): Scientific objectives. *Adv. Space Res.*, *36*, 989-995. doi: 10.1016/j.asr.2005.04.115

Russell III, J. M., Mlynczak, M. G., Gordley, L. L., Tansock, J. J., Jr., & Esplin, R. W. (1999). Overview of the SABER experiment and preliminary calibration results. *Proc. SPIE*, *3756*, 277-288. doi: 10.1117/12.366382

Sato, K. (1993). Small-scale wind disturbances observed by the MU radar during the passage of Typhoon Kelly. *J. Atmos. Sci.*, *50*(4), 518-537.

Sato, K., Watanabe, S., Kawatani, Y., Tomikawa, Y., Miyazaki, K., & Takahashi, M. (2009, OCT 7). On the origins of mesospheric gravity waves. *Geophys. Res. Lett.*, *36*. doi: 10.1029/2009GL039908

Sato, K., Yamamori, M., Ogino, S. Y., Takahashi, N., Tomikawa, Y., & Yamanouchi, T. (2003). A meridional scan of the stratospheric gravity wave field over the ocean in 2001 (MeSSO2001). *J. Geophys. Res.*, *108*(4491). doi: 10.1029/2002JD003219

Savitzky, A., & Golay, M. J. E. (1964). Smoothing and differentiation of data by simplified least squares procedures. *Analytical Chemistry*, *36*(8), 1627-1639. Retrieved from `http://dx.doi.org/10.1021/ac60214a047` doi: 10.1021/ac60214a047

Scinocca, J. F., & McFarlane, N. A. (2000). The parametrization of drag induced by stratified flow over anisotropic orography. *Quarterly Journal of the Royal Meteorological Society*, *126*(568), 2353-2393. doi: https://doi.org/10.1002/qj.49712656802

Scinocca, J. F., McFarlane, N. A., Lazare, M., Li, J., & Plummer, D. (2008). Technical note: The cccma third generation agcm and its extension into the middle atmosphere. *Atmos. Chem. Phys.*, *8*(23), 7055–7074. doi: 10.5194/acp-8-7055-2008

Shapiro, L. G., & Stockman, G. C. (2001). *Computer vision* (Vol. 3). Prentice Hall New Jersey.

Smith, R. B., Nugent, A. D., Kruse, C. G., Fritts, D. C., Doyle, J. D., Eckermann, S. D., . . . Beaton, S. (2016, JUL). Stratospheric Gravity Wave Fluxes and Scales during DEEPWAVE. *J. Atmos. Sci.*, *73*(7), 2851-2869. doi: 10.1175/JAS-D-15-0324.1

Stober, G., Sommer, S., Rapp, M., & Latteck, R. (2013). Investigation of gravity waves using horizontally resolved radial velocity measurements. *Atmos. Meas. Tech.*, *6*(10), 2893–2905. Retrieved from `http://www.atmos-meas-tech.net/6/2893/2013/` doi: 10.5194/amt-6-2893-2013

Strube, C., Preusse, P., Ern, M., & Riese, M. (2021). Propagation paths and source distributions of resolved gravity waves in ECMWF-IFS analysis fields around the southern polar night jet. *Atmospheric Chemistry Phys.*, *21*(24), 18641–18668. doi: 10.5194/acp-21-18641-2021

Thurairajah, B., & Cullens, C. Y. (2022, JUN 16). On the downward progression of stratospheric temperature anomalies using long-term SABER observations. *J. Geophys. Res. Atmos.*, *127*(11). doi: 10.1029/2022JD036487

Torrence, C., & Compo, G. P. (1998). A practical guide to wavelet analysis. *Bulletin of the American Meteorological Society*, *79*(1), 61 - 78. doi: 10.1175/1520-0477(1998)079⟨0061:APGTWA⟩2.0.CO;2

Trinh, Q. T., Kalisch, S., Preusse, P., Ern, M., Chun, H.-Y., Eckermann, S. D., . . . Riese, M. (2016). Tuning of a convective gravity wave source scheme based on hirdls observations. *Atmos. Chem. Phys.*, *16*, 7335-7356. doi: 10.5194/acp-16-7335-2016

Ungermann, J., Blank, J., Lotz, J., Leppkes, K., Hoffmann, L., Guggenmoser, T., . . . Riese, M. (2011). A 3-D tomographic retrieval approach with advection compensation for the air-borne limb-imager GLORIA. *Atmos. Meas. Tech.*, *4*(11), 2509-2529. Retrieved from `http://www.atmos-meas-tech.net/4/2509/2011/` doi: 10.5194/amt-4-2509-2011

Ungermann, J., Kaufmann, M., Hoffmann, L., Preusse, P., Oelhaf, H., Friedl-Vallon, F., & Riese, M. (2010). Towards a 3-D tomographic retrieval for the air-borne limb-imager GLORIA. *Atmos. Meas. Tech.*, *3*(6), 1647-1665. doi: 10.5194/amt-3-1647-2010

Vincent, R., & Alexander, M. (2000, JUL 27). Gravity waves in the tropical lower stratosphere: An observational study of seasonal and interannual variability. *J. Geophys. Res. Atmos.*, *105*(D14), 17971-17982. doi: 10.1029/2000JD900196

Wagner, J., Doernbrack, A., Rapp, M., Gisinger, S., Ehard, B., Bramberger, M., ... Hoor, P. (2017, MAR 24). Observed versus simulated mountain waves over scandinavia-improvement of vertical winds, energy and momentum fluxes by enhanced model resolution? *Atmos. Chem. Phys.*, *17*(6), 4031-4052. doi: 10.5194/acp-17-4031-2017

Weinreb, M. P., & Neuendorffer, A. C. (1973). Method to apply homogeneous-path transmittance models to inhomogeneous atmospheres. *J. Atmos. Sci.*, *30*, 662-666. doi: 10.1175/1520-0469(1973)030⟨0662:MTAHPT⟩2.0.CO;2

Worthington, R. M. (1999). Alignment of mountain wave patterns above wales: A vhf radar study during 1990-1998. *J. Geophys. Res.*, *104*, 9199-9212.

Wrasse, C. M., Nakamura, T., Takahashi, H., Medeiros, A. F., Taylor, M. J., Gobbi, D., ... Admiranto, A. G. (2006). Mesospheric gravity waves observed near equatorial and low-middle latitude stations: wave characteristics and reverse ray tracing results. *Ann. Geophys.*, *24*, 3229-3240.